


Topology of multiple cross-linked Su-Schrieffer-Heeger chains

A. Sivan* and M. Orenstein

Andrew and Erna Viterbi Faculty of Electrical and Computer Engineering, Technion—Israel Institute of Technology, Technion City, Haifa 3200003, Israel (Received 16 February 2022; revised 27 June 2022; accepted 12 August 2022; published 24 August 2022)

In polymer science, cross-linking of polymer chains yields a substantially modified system compared with the one-dimensional (1D) constituent chains, due to the increase of dimensionality and effective seeding by defects (cross-linking sites). Inspired by this concept, we analyze topological features of a unit cell of a generalized topological mesh comprised of several 1D Su-Schrieffer-Heeger (SSH) lattices cross-linked via a single site. The coupling site functions as a defect with protected states in the trivial regime and induces edges inside the bulk with protected localized states centered around it in the topological regime. When more than two lattices are coupled by the defect, namely, a graph dimensionality larger than one, the crossed chains support two types of localized eigenstates around the defect. One type is highly controllable by modifying the cross-linking strength, enabling broad tuning of eigenenergies from being submerged in the bulk band to becoming highly isolated and protected. We show that these unique features can be explained by an equivalence of the system to an SSH chain coupled nonreciprocally to an external reservoir, yielding a unique pseudospectrum for both the bulk and localized states, with spatially symmetric eigenstates. Applying non-Hermiticity by adding gain and loss to alternating sites, relevant, for example, to a possible realization of topological coupled-laser fabric, we observe an abrupt transition of the topologically protected midgap state from antilocalized to localized near the defect. By changing the gain-loss parameters, we observe a cascaded spatial symmetry breaking of the supported states at exceptional points where parity-time symmetry is broken, for both the localized and the bulk states, exhibiting various phases.

DOI: [10.1103/PhysRevA.106.022216](https://doi.org/10.1103/PhysRevA.106.022216)**I. INTRODUCTION**

Topology of structures and states has applications in many fields in physics. Originating from the concepts of topological insulators in solid-state physics and the quantum Hall effect [1,2], it has been shown that the idea of bulk-edge correspondence and its relation to parity-time (PT) symmetries [3] are also applicable to photonics [4–6]. Various structures that exhibit interesting topological phases have attracted attention, including the Su-Schrieffer-Hegger (SSH) model [7], the Aubry-Andre-Harper (AAH) model [8–10], and the Haldane model [11], to name only few examples. Much research has also been done on realization of topological effects in optical or photonic elements [12–18], with recent experiments demonstrating topological insulator lasers [19,20] and recently coherent lasing along the interface between two-dimensional (2D) topological arrays of vertical-cavity surface-emitting lasers [21].

Various extensions of lattice models and their topological characteristics have been studied. Non-Hermiticity was introduced to the SSH lattice by addition of onsite gain and loss or by imaginary and/or nonreciprocal couplings between sites, which resulted in richer physical phenomena including generalized topological phases attributed to the PT -symmetry operator [14,15,22–32], non-Hermitian skin effect [33–38], and more. Research of the topological effects and

phases of an SSH lattice in 2D was also conducted, generalizing the one-dimensional (1D) bulk-edge correspondence to higher dimensions and demonstrating the emergence of higher-order protected edges [39–46]. Other extensions with nonlocal couplings and other symmetries were also reported [47–51].

The effects of defects and discontinuities on the states and dynamics of SSH lattices have been considered in the literature. It has been suggested that the incorporation of either one or more sites that differ from the embedding lattice or on the interface between distinct lattices introduces states with unique characteristics such as localization and topology-induced robustness against noise [12,13,52–62]. These defects enrich the dynamics of the pure lattices and can be used to tailor desired eigenspectra and eigenstates. However, these works are reported primarily in a 1D framework, and defects in higher-dimensional systems were not rigorously studied. This is a considerable gap in the understanding of the effects lattice defects have on realistic topological arrays.

In this paper, we study the influence of defects on the dynamics of lattices with a dimension higher than one. A plausible scheme for gradually increasing the dimensionality is to form a crosshatched network of SSH chains coupled at each intersection point, while reducing the distance between those intersections. Here, we present a rigorous analysis of a building block of such a network, consisting of several crossed SSH lattices coupled by a single mutual defect site in both the Hermitian and non-Hermitian regimes. The model is general to any number of similar or dissimilar lattices, and in this

*amirsi@campus.technion.ac.il

paper, we focus for concreteness on the simple crossed-chain structure—a structure consisting of four identical 1D SSH lattices connected to a mutual coupling element. This configuration spans more than 1D (as will be further explained in Sec. II), and the defect site acts as a source for the generation of induced edges in the mutual boundaries of the four 1D topological lattices. This produces several key results. In the trivial regime, we find two different types of localized states that are supported by this structure, while in 1D, only one type is resolved, unless a more complex defect is included (see Sec. III). We denote those two types as the defect (induced) states and the zero-energy state. The former has energies residing outside of the bulk pseudospectrum, while the latter is a midgap state with zero energy as imposed by symmetry considerations. In the topological regime the zero-energy state becomes antilocalized, and a third type of localized state exists, which is the well-known topological edge state of free SSH chains. We show that the crossed-chain system can be described by three identical disconnected SSH lattices and a fourth SSH lattice coupled to an effective external reservoir via a nonreciprocal coupling. The latter constitutes an energy ladder shifted from that of a free SSH chain for both the localized and bulk states that are associated with the defect coupling. Those states are shown to be spatially symmetric. The system is then extended to a non-Hermitian setup by adding onsite imaginary potentials in a symmetry-preserving scheme, describing gain and loss. We find that, although gain and loss were added, the defect-associated states have the same wave numbers as in the Hermitian case. Furthermore, we show how the spatial symmetries of the amplitudes of the eigenstates break in a sequence of exceptional points. Our proposed framework therefore expands the understanding of the influence of defects in higher dimensions and suggests that they can be exploited to control the dynamics of a higher-dimensional system. As mentioned, the crossed-chain structure can be used as a building block to create a fully 2D protected state by effectively creating an array of internal edges within the lattice bulk, rather than the more classical 1D protected edge states along the boundary walls between different 2D lattices.

The paper is organized as follows. In Sec. II, we present the Hermitian crossed-chain SSH structure and emphasize the dynamics introduced by the higher dimensionality of the system. In Sec. III, we rigorously analyze the effect of the defect coupling strength on the energy pseudospectrum of the structure. In Sec. IV, we generalize our framework by adding non-Hermiticity to the system. We conclude and further discuss the results in Sec. V.

II. THE HERMITIAN CROSSED-CHAIN SSH CONFIGURATION

The Hermitian crossed-chain configuration is comprised of K finite SSH chains connected to a mutual additional lattice element, as depicted in Fig. 1(a) for the case of $K = 4$ identical chains. We will henceforth refer to this additional element as the defect site. In this section, we explore the case of a basic defect that we will soon define. Scattering-theory methods such as Schwinger-Lippmann may be useful when considering simple lattices and some extensions [63–69] but

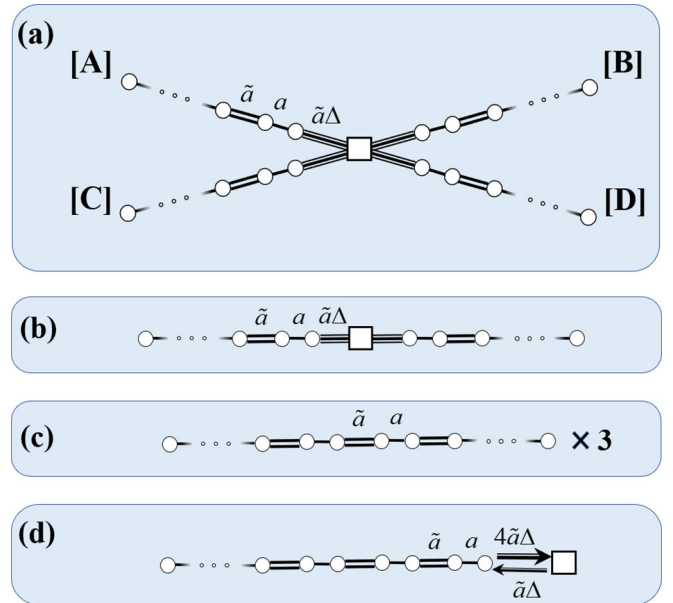


FIG. 1. (a) Schematic illustration of the symmetric crossed-chain configuration. Black lines denote coupling strength a , double lines the coupling strength \tilde{a} , and triple lines the defect coupling strength $\tilde{a}\Delta$. (b) One-dimensional (1D) mirrored Su-Schrieffer-Heeger (SSH) chain structure that was analyzed in, e.g., Ref. [16]. The configuration of (a) is isospectral with (c) + (d). (c) The degenerate triplet eigenvalues are equivalent to those of three detached SSH chains of the same length and coupling coefficients as these of its constituent chains, and (d) the eigenvalues of the singlet eigenvalues are equivalent to those of the same SSH chain connected to an additional element via a nonreciprocal coupling strength.

are generally intractable when schemes that are more complicated are considered. We will therefore solve the Hamiltonian eigenvalue problem directly.

The Hamiltonian of a single Hermitian SSH chain indexed by σ and formed by $M_\sigma \in 2\mathbb{N}$ sites with a unit distance between them is

$$H_\sigma = \sum_j^{M_\sigma-1} a_j^\sigma \phi_j^{\sigma\dagger} \phi_{j+1}^\sigma + \text{H.c.}, \quad (1)$$

$$a_j^\sigma = \begin{cases} a^\sigma & \forall j \in 2\mathbb{N} \\ \tilde{a}^\sigma & \forall j \in 2\mathbb{N} + 1 \end{cases} \quad (2)$$

Here, ϕ_j^σ are the amplitudes at the j th site, H.c. denotes the Hermitian conjugate, and a^σ and \tilde{a}^σ are the respective intracell and intercell coupling coefficients that are assumed to be real and positive. The crossed-chain SSH structure [Fig. 1(a)] is an intersection of four SSH chains of lengths M_σ with $\sigma \in \{A, B, C, D\}$, as defined by Eq. (1), through a connection to a common site described by a defect site term U , such that

$$H_{\text{tot}} = U + \sum_\sigma \sum_j^{M_\sigma-1} a_j^\sigma \phi_j^{\sigma\dagger} \phi_{j+1}^\sigma + \text{H.c.}, \quad (3)$$

$$U = \sum_\sigma \tilde{a}^\sigma \Delta^\sigma \phi_{M_\sigma}^{\sigma\dagger} \phi_\Delta + \text{H.c.}, \quad (4)$$

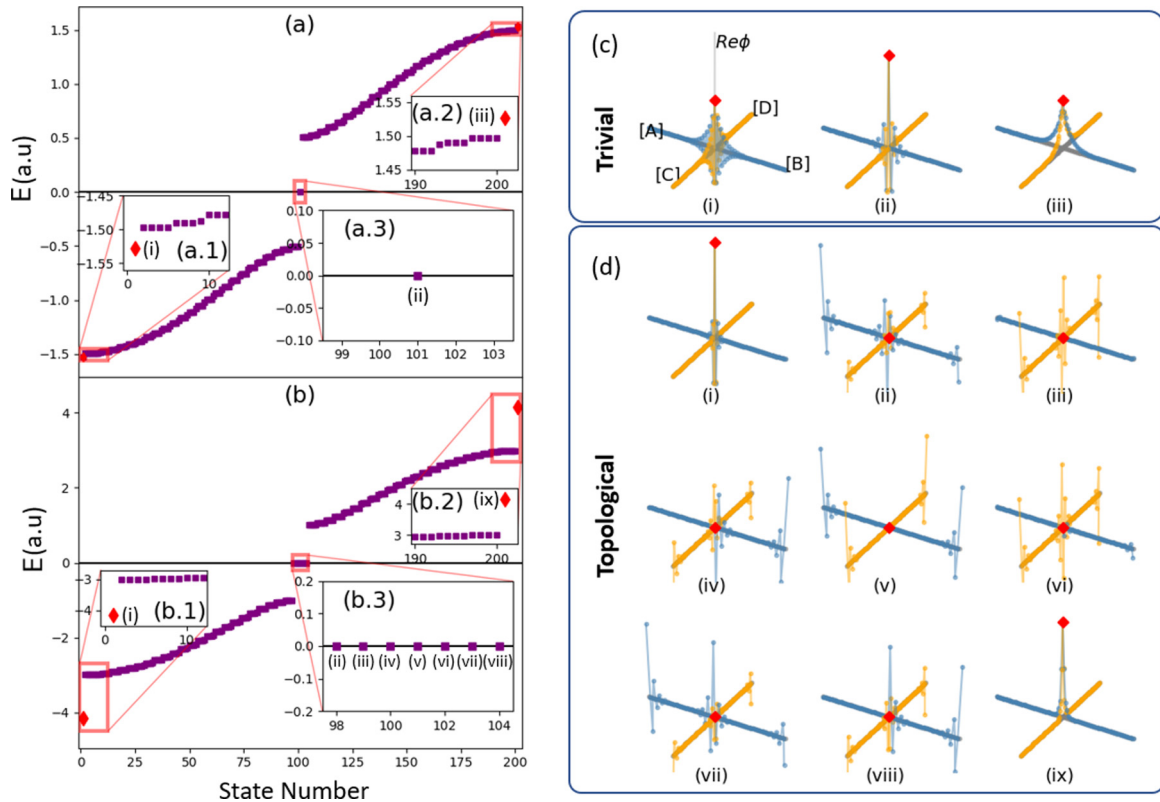


FIG. 2. Energy pseudobands for symmetric crossed-chain structures with $M = 50$ and $a = 1$. (a) Trivial Su-Schrieffer-Heeger (SSH) chains with $\tilde{a} = 1/2$. (b) Topological SSH chains with $\tilde{a} = 2$. The insets (a.1)–(a.3) and (b.1)–(b.3) are magnified portions of the pseudospectra. Nonmidgap localized states are marked with red diamonds. Insets (a.3) and (b.3) are zero-energy and edge states. (c) and (d) Amplitudes of the localized states in the crossed-chain structure, with SSH chains [A] through [D], numbered in an ascending order with respect to energy. (c)(i)–(c)(iii) The localized states for the trivial case (a); (c)(i) and (c)(iii) are the nonmidgap defect states, (c)(ii) is the zero-energy state. (d)(i)–(d)(ix) The localized states for the topological case (b); (d)(i) and (d)(ix) are the localized defect states, (d)(v) is the defect zero energy state localized on the outer edges of the structure, (d)(ii)–(d)(iv) and (d)(vi)–(d)(viii) are the edge states localized on the edges of the constituent SSH chains. Red diamonds mark the defect site amplitudes in (c) and (d).

where the coupling strength of the defect to the end of the σ SSH chain is $\tilde{a}^\sigma \Delta^\sigma$, and the defect site amplitude is ϕ_Δ . In contrast to a 1D system consisting of two SSH chains around a defect in a mirrored setting [Fig. 1(b)], which was treated in previous works (e.g., Refs. [12,13,16]), the crossed-chain structure has more than 1D. The measure of dimensionality in our case is borrowed from graph theory: a star graph (the defect is the central node and the SSH chains are the leaves) is 1D for $K \leq 2$ and 2D for $K > 2$. This definition is different from geometrical 2D (e.g., the 2D SSH lattice in Ref. [39]).

We define a *basic defect* as a site that acts as a boundary wall between the K SSH lattices, with $\Delta^\sigma = \Delta = 1$ for every σ . This defect is basic in the sense that it only acts as a boundary wall between several lattices, but it does not modify the coupling scheme of any of them. Systems with a nonbasic defect ($\Delta \neq 1$) will be addressed in the next sections. Furthermore, from this point on, we will discuss only *isotropic* systems with $K = 4$, wherein $M^\sigma = M$, $a^\sigma = a$, and $\tilde{a}^\sigma = \tilde{a}$ for all σ .

The increase in dimensionality introduces new features that are absent from the 1D case.

The first feature, occurring in the topologically trivial regime, is that additional localized states are now sup-

ported by the system. While the trivial 1D structure (for which $K = 2$) contains one localized defect state, the trivial crossed-chain structure has three nondegenerate localized defect states. In Fig. 2(a), we illustrate the pseudospectrum of a crossed-chain structure in the trivial regime, with insets focusing on the localized defect states depicted in Figs. 2(c)(i)–2(c)(iii). One of the localized defect states has zero energy with a localization length of $\eta_0 = -\ln(\tilde{a}/a)$ and is localized on the defect [Figs. 2(c)(ii)], as in the 1D case [12], while two localized defect states appear with energies given by

$$E_\Delta^2 = a^2 + \tilde{a}^2 + 2a\tilde{a} \cosh \kappa, \quad (5)$$

where the localization length $\kappa \in \mathbb{R}^+$ is related to the parameters of the structure by

$$K = 1 + \frac{a}{\tilde{a}} e^\kappa \quad (6)$$

(Appendix A). These two states are also localized on the defect site itself. Equation (6) has a solution for κ in the trivial regime $\tilde{a} < a$ if and only if $K > 2$. Therefore, while the zero-energy defect state (henceforth denoted as E_0) stems from the symmetry of the structure and exists in the 1D case, the emergence of these two additional localized defect states

is a feature attributed to the higher dimensionality of the system.

The second important feature of the higher dimensionality occurs in the topological regime $\tilde{a} > a$ and is the distinction of the regular edge states from the localized defect states and zero-energy state, in terms of their localization lengths.

The topological regime here is obtained under the same coupling relations as for the isolated SSH chain ($\tilde{a} > a$). Although rigorous calculation of the topological invariant (e.g., Chern number) of our aperiodic structure is a formidable task, the transition from a trivial to a topological phase is clear and exhibits the typical edge-bulk correspondence and chiral symmetry breaking at the bandgap closing [70,71]. The chiral symmetry is consistent with the relation $\sigma_z H_{\text{tot}} \sigma_z = -H_{\text{tot}}$ that is fulfilled for the matrix σ_z generalized from its definition in Ref. [16] and is indicated by the fact that the eigenvalues of the system come in $(-E_m, E_m)$ pairs, as we explicitly show in the next section.

In the topological regime, we get two localized defect states $\pm E_\Delta$ and seven other localized edge states inside the bulk gap [Fig. 2(b)]. The seven localized states [Figs. 2(d)(ii)–2(d)(viii)] are further separated to one zero-energy state E_0 [Fig. 2(d)(v)] and six other edge states E_E . Similar states were briefly mentioned in analyses of 1D systems in the topological regime [72,73]; however, even for the 1D system, no rigorous exploration has been conducted, and thus, we provide a concise derivation in Appendix E. The zero-energy state E_0 is a symmetric state with a localization length $\eta_0 = |\ln(a/\tilde{a})|$, antilocalized with respect to the defect site. The E_E states are showing mixed localization, both on the outer edges and on the emerging induced edges neighboring with the defect site. These states exhibit exponential localization only in the long-lattice limit, with localization length $\eta_E \approx -\ln(a/\tilde{a})$ [74]. In other words, while the energy of E_0 is identically zero and its amplitude profile is exactly exponential for all lengths and lattice coefficients, the energies of the states E_E only approach zero and an exponential localization for a long lattice. In this paper, we employ system parameters for which the long lattice approximation $\eta_E \approx -\ln(a/\tilde{a})$ holds.

When solving Eq. (6) in the topological regime, one can see that $K = 2$ yields $\kappa = -\ln(a/\tilde{a})$, which means that the localization lengths of the localized defect state and of the topological edge states are equal in 1D. For a higher-dimensional system ($K > 2$), the localized defect states $\pm E_\Delta$ have different localization lengths from those of the edge states. This result indicates that, in a higher-dimensional system, the state localization due to the topological nature of the SSH chains is a distinct physical phenomenon from the state localization due to the presence of the defect.

We have thus shown that, in the crossed SSH trivial regime, nonmidgap localized states emerge because of the effective (internal) edge induced by the coupling defect. This type of state does not exist in the previously researched $K = 2$ structure in the trivial case. We have thus observed three different types of localized states—the zero-energy state E_0 and the localized defect states $\pm E_\Delta$ that originate from the defect, both of which exist also in the trivial regime, and in addition, the edge states E_E that are due to the topology of the SSH chains in the topological regime.

III. CONTROLLING PROTECTED STATES BY TUNING OF DEFECT COUPLING

We analyze the effect of modifying the effective defect coupling strength Δ on the pseudospectrum and eigenstates of the system, generalizing the results of the previous section to more complicated defects. The observation that the coupled cross-chain system is isospectral with an equivalent system consisting of two manifolds—one is a *degenerate trivial system* made of $K-1$ simple uncoupled SSH chains [Fig. 1(c)], and the second is a single SSH lattice coupled to a nonreciprocal edge element [Fig. 1(d)]—is a cornerstone in our analysis. This will be further explained and proven. Furthermore, for some values of $\Delta \neq 1$, one can find localized states, with localization lengths that were exhibited in Sec. II only for the 2D case, in the 1D ($K = 2$) settings.

Starting with the extreme case of $\Delta = 0$, the system is comprised of four identical disconnected SSH chains and a single isolated defect site, and so the pseudospectrum is quadruply degenerate plus one. In the trivial regime, there is only one localized state—the zero-energy state residing on the defect site. In the topological regime there are nine localized states—two edge states of each of the identical topological SSH chains and one zero-energy state completely localized on the defect. The nonzero energies are related to a discrete wave number k_m via the well-known SSH lattice dispersion relation $E^2(k_m) = a^2 + \tilde{a}^2 + 2a\tilde{a} \cos k_m$ in both the trivial and topological regimes.

For the general case $\Delta > 0$, the aforementioned decomposition is manifested, as the quadruply degenerate bulk pseudospectrum with energies $E_m(k_m)$ breaks into two manifolds—a triplet: a triply degenerate pseudospectrum with energies $E_T(k_m) = E_m(k_m)$; and a singlet: a pseudospectrum with shifted (relative to the free SSH) eigenenergies $E_S(p_m)$ and shifted wave numbers $p_m \equiv k_m + \delta k_m$ [Fig. 3(a)]. The transformation of each degenerate quartet into a degenerate triplet and a singlet state with shifted energies and wave numbers results, as may be expected, from coupling of the SSH chains to the defect.

The bulk energy of the m th triplet is given by $E_T^2(k_m) = a^2 + \tilde{a}^2 + 2a\tilde{a} \cos k_m$ (Appendix B) which is the energy of the m th state of an isolated single SSH chain [Fig. 1(c)]. In the topological regime, this manifold also includes a triply degenerate pair of topological edge states E_E on the edges of the chains with localization lengths $\eta_E \approx -\ln(a/\tilde{a})$ that do not depend on Δ . In the triplet manifold, since the energy of the bulk states $E_T(k_m)$ is equal to the energy of the bulk states of a free SSH chain $E_m(k_m)$, each m th triplet state is comprised of three degenerate superpositions of the m th bulk states of the four SSH chains. Additionally, since the free SSH chains do not include the defect site, the defect site amplitude in the triplet states must be zero. The singlet bulk state shifted from the m th band must be spatially symmetric with respect to the central element [Fig. 3(b)]. Moreover, the energy shift of the singlet bulk is related to a wave number shift which, as shown in Appendix B, implies a nonzero amplitude on the defect site together with the symmetrical extended amplitude profile on the chains.

The singlet part of the pseudospectrum is more interesting since it unfolds the impact of the defect and can be obtained

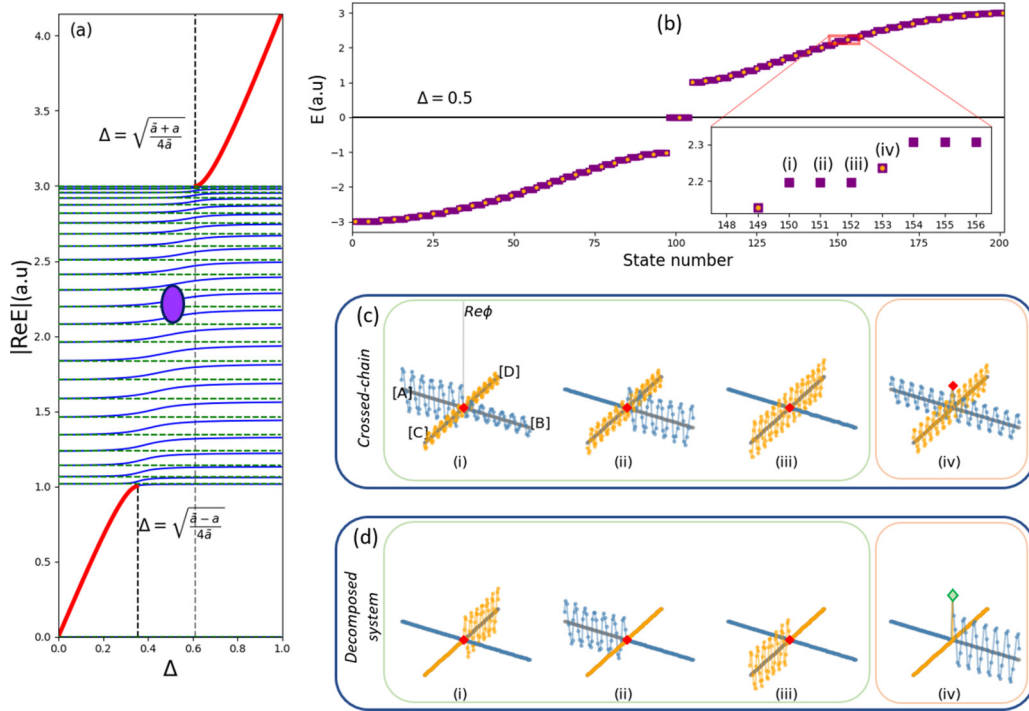


FIG. 3. (a) Positive real-energy pseudospectrum for the symmetric crossed-chain system of Fig. 1(a) in the topological regime with $\tilde{a} = 2a$ and $M = 50$ vs defect coupling strength coefficient Δ . Dashed green lines denote the energy levels of the triplet pseudospectrum, blue lines denote the energy levels of the singlet pseudospectrum, and the thick red lines denote the isolated localized defect states. Vertical dashed lines mark the critical values of Δ between which the localized defect states are merged into the bulk. (b) Energy pseudospectrum at $\Delta = 0.5$ [the purple marker in subfigure (a)]. The yellow dots mark the singlet pseudospectrum. Inset: An example triplet bulk states [marked (i)–(iii)] and the associated singlet state [marked (iv)]. Real values of the amplitudes of the states marked in this inset appear for (c) the crossed-chain system and (d) the reduced representation by an isospectral system comprised of three detached Su-Schrieffer-Heeger (SSH) chains and one SSH chain coupled nonreciprocally to a defect site. Defect site amplitude marked by a red diamond, and the amplitude of the nonreciprocally coupled defect is marked by a light-green diamond.

from analyzing an equivalent non-Hermitian system. Since the singlet states are symmetric around the defect site, in the reduced representation, we consider an effective system comprised of a single SSH chain connected to an external reservoir with a coupling constant $\tilde{a}\Delta$ [Fig. 1(d)]. However, since the defect site in the crossed-chain structure experiences coupling to four identical adjacent sites, the reservoir in the effective system is coupled back to the effective SSH lattice with a coupling strength of $4\tilde{a}\Delta$. This introduces non-Hermiticity to the Hamiltonian of the effective system, although it still supports only real eigenenergies. The bulk energies of the singlet manifold are given by

$$E_S^2(p_m) = a^2 + a\tilde{a} \frac{\sin[p_m(\frac{M}{2} - 1)]}{\sin(p_m \frac{M}{2})} + 4(\Delta\tilde{a})^2, \quad (7)$$

and the wave numbers $p_m = k_m + \delta k_m$ are the solutions of an implicit equation derived in Appendix B. It should be noted that, since Eq. (7) is an even function, its solutions are $(-E_S, E_S)$ pairs. For defect coupling strengths of $\Delta^2 < (\tilde{a} - a)/4\tilde{a}$ and $\Delta^2 > (\tilde{a} + a)/4\tilde{a}$, the localized states emerge from the bulk with energies:

$$E_\Delta^2 = a^2 + \tilde{a}^2 - 2a\tilde{a} \cosh \kappa, \quad (8)$$

$$E_\Delta^2 = a^2 + \tilde{a}^2 + 2a\tilde{a} \cosh \kappa, \quad (9)$$

respectively (Appendix A). These are illustrated by the red curves in Fig. 3(a).

Unlike the localization lengths η_0 and η_E that do not depend on the defect strength Δ , in the defect-induced states, there is a clear dependence given by (Appendix A)

$$\Delta^2 = \frac{\tilde{a} + a\lambda(\kappa)^{-1}}{4\tilde{a}}, \quad (10)$$

where $\lambda(\kappa) = -e^{-\kappa}$ if the localized defect-state energies $\pm E_\Delta$ are within the gap ($|E_\Delta| < \tilde{a} - a$) and $\lambda(\kappa) = e^{-\kappa}$ if they are outside the bulk pseudospectrum ($|E_\Delta| > \tilde{a} + a$). The former exists only in the topological regime. Another state belonging to the singlet mode is trivial solution $E_S = 0$ which is the zero-energy state E_0 , localized on the defect site in the trivial regime and on the outer edges of the structure in the topological regime. Like the case of a basic defect, the zero-energy state E_0 has a localization length given by $\eta_0 = |\ln(a/\tilde{a})|$, independent of Δ for $\Delta \neq 0$.

We have shown that the Hermitian crossed-chain system can be fully described by an isospectral effective system that is a combination of a triply degenerate SSH lattice and a non-Hermitian system consisting of an SSH coupled to an external nonreciprocal reservoir. The energy pseudospectrum can therefore be denoted as $E(k, \Delta) = \{E_0, E_S(p_m, \Delta), 3E_T(k_m)\}$, with $m \in \pm\{1 \dots M/2\}$. We emphasize that this decomposition is exact and that the reduced representation of the system

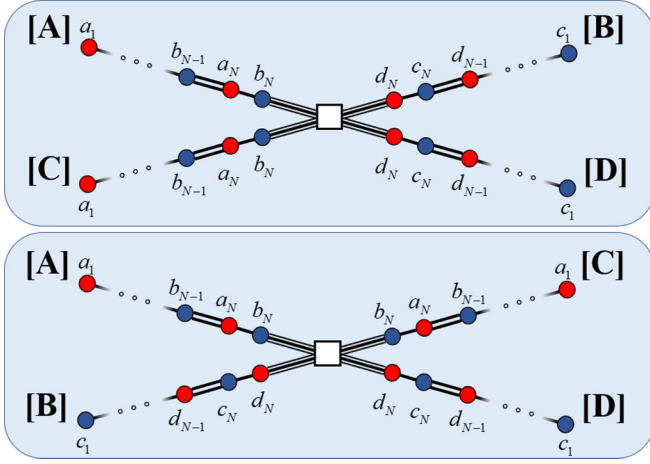


FIG. 4. Illustration of the symmetric non-Hermitian crossed-chain T -symmetric configuration. Red sites denote gain γ , and blue circles denote loss $-\gamma$. The two illustrations portray an identical system; the crossed-chain scheme can be analyzed as the systems comprised of chains $\{A, B\}$ and $\{C, D\}$, or chains $\{A, C\}$ and $\{B, D\}$, coupled through the defect site.

and original representation of Eq. (3) are spectrally equivalent. Here, $E(k, \Delta)$ is comprised of $(-E_m, E_m)$ pairs and a zero-energy state, indicating the chiral symmetry mentioned in Sec. II.

This degeneracy breaking into singlet and triplet manifolds can be easily generalized to the K -chains case in which the pseudospectrum splits into a singlet and $(K-1)$ -fold-degenerate manifolds. This is observable only in systems of dimensionality higher than one since, in the 1D system ($K = 2$), the splitting of a degenerate doublet pseudospectrum is into two distinct singlet manifolds; in one manifold, the extended amplitude distributions are antisymmetric with wave number k_m and, in the other, are symmetric with wave number $k_m + \delta k_m$ and a nonzero amplitude on the defect. Therefore, no degeneracy occurs.

IV. NON-HERMITIAN CROSSED-CHAINS

A. Model of the non-Hermitian structure

We generalize the crossed-chain Hamiltonian to a non-Hermitian setting, by introducing imaginary on-site potentials describing loss and gain. For concreteness, we studied the case of an alternating gain-loss pattern along each of the four coupled chains, with a transparent defect. The complex SSH Hamiltonian is

$$H_\sigma = i \sum_j^{M_\sigma} \gamma_j^\sigma \phi_j^{\sigma\dagger} \phi_j^\sigma + \sum_j^{M_\sigma-1} a_j^\sigma \phi_j^{\sigma\dagger} \phi_{j+1}^\sigma + \text{H.c.}, \quad (11)$$

with the nondiagonal coefficients generally defined as in Eq. (2), and $\gamma_j^\sigma = (-1)^j \gamma^\sigma$, $\gamma^\sigma \in \mathbb{R}^+$ are the gain-loss coefficients. For characterizing our system, we employ parity (P), time (T), and parity-time (PT) symmetries. While the conventional definition of the time-reversal operator $T(-i)T^{-1} = i$ is directly applicable in our system, attempting to generalize P and PT symmetries to the crossed-chain configuration is not trivial; the definition of P symmetry is not unique for a struc-

ture that is not 1D since the system cannot be described by a single spatial axis. Our parity operator is *unbroken* if the system is invariant under permutation of any of the K SSH chains (this coincides with the usual definition $PxP^{-1} = M+1-x$ for the case of 1D). We use the notation PT symmetry more loosely for indicating a situation where the eigenenergies are real (quasi-Hermitian operator) [3].

For $\forall \sigma : M_\sigma = M$, $a^\sigma = a$, $\tilde{a}^\sigma = \tilde{a}$, $\gamma^\sigma = \gamma$, as demonstrated in Fig. 4, the crossed-chain system can be analyzed either as two SSH systems, each maintaining PT symmetry (but not P symmetry) coupled by a defect, or as two SSH systems, each preserving P symmetry but breaking PT symmetry, coupled by the same defect. This ambivalence stems from the dimensionality imposed by the coupling through the defect site and has no 1D equivalence.

We denote, without loss of generality, $\gamma_j^{A,C} = (-1)^j \gamma^{A,C}$ and $\gamma_j^{B,D} = -\gamma_j^{A,C}$. Rewriting Eq. (3) cf. Eq. (4) to include the non-Hermiticity yields

$$H_{\text{tot}, \gamma} = \sum_\sigma \tilde{a}^\sigma \Delta^\sigma \phi_{M_\sigma}^{\sigma\dagger} \phi_\Delta + \sum_\sigma \sum_j^{M_\sigma} (-1)^j i \gamma^\sigma \phi_j^{\sigma\dagger} \phi_j^\sigma + \sum_\sigma \sum_j^{M_\sigma-1} a_j^\sigma \phi_j^{\sigma\dagger} \phi_{j+1}^\sigma + \text{H.c.} \quad (12)$$

As in the previous sections, we will consider the isotropic case $\forall \sigma : M_\sigma = M$, $a^\sigma = a$, $\tilde{a}^\sigma = \tilde{a}$, $\gamma^{B/D} = \gamma$.

In general, topological protected states are expected to exhibit enhanced robustness to disorder of the lattice. This is a good indicator for a topological phase, especially for the non-Hermitian case where the other indicators such as topological invariants and bandgap closing are not well defined. We performed a thorough robustness analysis for all protected states in the topological phase of the non-Hermitian case under chirality- and PT -symmetry-preserving disorder (as was done before for similar cases, e.g., in Refs. [13,16]). The analysis detailed in Appendix G shows that, even for disorder parameters of $\sim 1 - \gamma/|\tilde{a} - a|$ (the maximal disorder of given parameters above which PT symmetry may be broken, as explained in the appendix), the variances of the distributions of numerically calculated wave numbers for the topological states in hundreds of realizations amount to $< 1.6\%$ of their respective mean values. This demonstrates substantial robustness for the zero states, edge states, and defect states, thereby validating the robustness of the non-Hermitian topological phase.

Unlike the Hermitian case, when the non-Hermiticity is introduced, the system is comprised of two identical pairs of complex-conjugate SSH chains rather than four identical SSH chains. Therefore, there are two possible choices of effective systems and SSH chains that are identical up to a complex-conjugation operation (Appendix D). Thus, although the amplitude profiles of the states are not identical on the four SSH chains, knowledge of the profile of one chain in a singlet state suffices to unambiguously describe the entire system. Moreover, since the full crossed-chain system and the reduced equivalent systems are all T symmetric, complex conjugation does not affect their pseudospectra. Thus, the effective system would yield valid isospectral representations of the system,

and we can use the equivalent system of one non-Hermitian SSH chain with nonreciprocal coupling to a reservoir and three non-Hermitian SSH chains.

The pseudospectrum of the system is $E(k, \Delta, \gamma) = \{E_0, E_{S,\gamma}(p_m, \Delta), 3E_{T,\gamma}(k_m)\}$ for $m \in \pm\{1 \dots M/2\}$, where $E_{S,\gamma}(p_m, \Delta)$ and $E_{T,\gamma}(k_m)$ are the gain-parameter-dependent singlet and triplet energies, respectively. It is interesting to note that the shifts in the wave numbers of the bulk states associated with the singlet state are exactly identical to those obtained for the Hermitian case, and do not depend on γ (Appendix D), making the result of the previous section much more general.

The bulk energies of the non-Hermitian system are given by

$$E_{T,\gamma}^2(k_m) = a^2 + \tilde{a}^2 + 2a\tilde{a} \cos k_m - \gamma^2, \quad (13)$$

$$E_{S,\gamma}^2(p_m, \Delta) = a^2 + \tilde{a}^2 + 2a\tilde{a} \cos p_m - \gamma^2, \quad (14)$$

for the non-Hermitian triplet and singlet manifolds, respectively, where k_m are the discrete wave numbers of a constituent SSH chain with $\gamma = 0$, and p_m are the discrete solutions of the implicit function as described in Sec. III.

The energies of the localized states are generalized to include the non-Hermiticity parameter γ (Appendix C). The defect states of the singlet manifold are

$$E_{\Delta,\gamma}^2 = a^2 + \tilde{a}^2 \pm 2a\tilde{a} \cosh \kappa(\Delta) - \gamma^2, \quad (15)$$

while the triplet topological edge states (in the long lattice limit) are

$$E_{E,\gamma}^2 = a^2 + \tilde{a}^2 - 2a\tilde{a} \cosh \eta_E - \gamma^2. \quad (16)$$

We show in Appendix C that the localization length κ of the localized defect states $\pm E_{\Delta}$ does not depend on γ but depends on Δ exactly as in the Hermitian case [see Eq. (10)]. The edge states in Eq. (16) exist of course only in the topological regime. In the Hermitian case, the edge localization length was given by $\eta_E \approx -\ln(a/\tilde{a})$, and it can be readily obtained from the Hamiltonian equations that η_E does not depend on γ . Substituting η_E in Eq. (16), we obtain that the energies of the edge states are $E_{E,\gamma} \approx \pm i\gamma$, which are purely imaginary.

We emphasize that the distinction between the localization constants of the edge states and defect states for a basic defect is a property of the higher dimensionality of the system, also when non-Hermiticity is introduced.

The third type of a localized state is the zero-energy state E_0 discussed in the previous sections. Its localization length is obtained from eliminating the left-hand side (LHS) of the non-Hermitian extension of the zero-energy state dispersion relation [16]:

$$\eta_0 = \eta_0(\gamma) = \text{arc cosh} \left(\frac{a^2 + \tilde{a}^2 - \gamma^2}{2a\tilde{a}} \right). \quad (17)$$

Recall that, in the Hermitian case, we obtain $\eta_E \approx \eta_0(\gamma = 0) = -\ln(a/\tilde{a})$ and $E_E \approx E_0 = 0$ in the long-lattice approximation. Therefore, an important signature of the non-Hermiticity in the topological regime is the further generation

of a distinction between the zero-energy state E_0 and the triply degenerate topological SSH edge states E_E .

We may wonder about the discontinuous characteristics of the localization between the Hermitian and the non-Hermitian cases when the addition of very small gain-loss ($\gamma \rightarrow 0^+$) prompts a very abrupt change in the spatial localization of the zero-energy state from the outer edges to the inner (defect induced) edges (Fig. 5). This abrupt transition is a consequence of the long-chain approximation; without this approximation, E_E is small but finite except at a specific small value of $\gamma = \gamma_s$ for which $E_E(\gamma_s) = 0$, and then the edge states are exactly degenerate with the zero-energy state. For $0 < \gamma < \gamma_s$, the zero-energy state is localized on the far edges of the SSH chains, but as γ is increased, localizations appear on the inner edges and increase in magnitude. At $\gamma = \gamma_s$, the amplitudes at the induced and outer SSH edges are equal up to a phase, and for $\gamma > \gamma_s$, the amplitudes become localized only on the induced edges around the defect. In the long-chain approximation, $\gamma_s \approx 0$, and thus, the transition is abrupt. As γ is further increased, the amplitude on the defect site increases until, at $\gamma = \tilde{a} - a$, the bulk energies coalesce in exceptional points, and the zero-energy state becomes delocalized. Further on, when the energies of the entire bulk become purely imaginary at $\gamma = \tilde{a} + a$ due to PT -symmetry breaking, as will be described in the next subsection, the zero-energy state becomes localized on the defect site itself.

B. Phase diagrams

Obviously, when the gain parameter γ is varied, the entire system goes through several phase transitions. Some of them are unique to the crossed-chain structure. We follow the phases of crossed-chain structures across the parameter ranges.

In both the trivial and topological regimes under the long-chain approximation, when $\gamma^2 \leq (a - \tilde{a})^2$, the bulk energies are purely real, indicating that the bulk is PT protected, and appear in pairs $(E_m, -E_m)$ for all m . As γ increases, the bulk energies of the states $E_{m,\gamma}$ approach zero as $\sim \pm \sqrt{E_m^2 - \gamma^2}$. When $E_m^2 = \gamma^2$, the bulk states $\pm E_{m,\gamma}$ coalesce at an exceptional point, and their energies become a conjugate pair of purely imaginary values, so that PT symmetry is gradually broken along a series of exceptional points until the entire bulk is purely imaginary at $\gamma = (a + \tilde{a})^2$. The zero-energy state E_0 remains pinned at zero for all values of γ . We denote the PT -symmetric, partially broken, and broken regimes as phases I, II, and III, respectively.

In the trivial region, the localized defect state pair $\pm E_{\Delta}$ exists for $\Delta^2 > (\tilde{a} + a)/4\tilde{a}$ [Fig. 6(a)]. From Eq. (15), this pair coalesces and becomes purely imaginary at $\gamma = |E_{\Delta}|$. Above this value, the entire pseudospectrum of the system is purely imaginary, and PT symmetry is broken. However, for $(a + \tilde{a})^2 < \gamma < |E_{\Delta}|$, there exist protected localized states that maintain PT symmetry, while the entire bulk is PT broken. This unique phase, denoted IIIA, does not exist in the case of a 1D system with a basic defect and is a result of the higher dimensionality of the crossed-chain system for $\Delta = 1$.

For $(\tilde{a} - a)/4\tilde{a} < \Delta^2 < (a + \tilde{a})/4\tilde{a}$ [Fig. 6(b)], no localized defect state exists, and the PT symmetry of the entire structure is determined solely from the bulk.

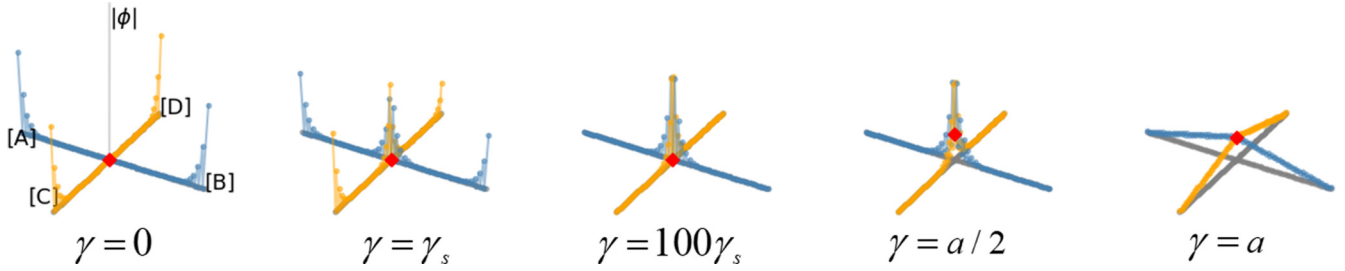


FIG. 5. The zero-energy state in the topological regime for different values of γ with Su-Schrieffer-Heeger (SSH) parameters $a = 1$, $\tilde{a} = 2$ and $M = 50$. The transition from outer- to inner-edge localization occurs under these conditions for $\gamma_s \approx 4.4 \times 10^{-8}$, which is virtually zero. The transition is even more abrupt when further increasing the chain lengths.

In the topological regime [Figs. 6(c)–6(e)], for $\Delta \neq 0$, there are three degenerate pairs of edge states that, in the long chain approximation, have conjugate imaginary energies [given in Eq. (16)] for $\gamma > 0$. These three pairs of states, illustrated in Fig. 6(f), consist of amplitudes localized on the four chain edges on which there is gain (loss), with an energy of $E_E = i\gamma$ ($E_E = -i\gamma$). Therefore, the system is never fully PT symmetric in the topological regime. We denote the bulk PT -symmetric, partially broken, and broken

regimes in the topological regime as phases I_T , II_T , and III_T , respectively.

For $\Delta^2 > (a + \tilde{a})/4\tilde{a}$ [Fig. 6(c)], there are localized defect states E_Δ that coalesce at $(a + \tilde{a})^2 < \gamma = |E_\Delta|$, above which the entire system is PT -symmetry broken. For $(a + \tilde{a})^2 < \gamma < |E_\Delta|$ (phase III_{AT}), only the localized defect states are PT symmetric, whereas both the bulk and topological edge states are PT broken.

For $(\tilde{a} - a)/4\tilde{a} < \Delta^2 < (a + \tilde{a})/4\tilde{a}$ [Fig. 6(d)], no localized defect states exist.

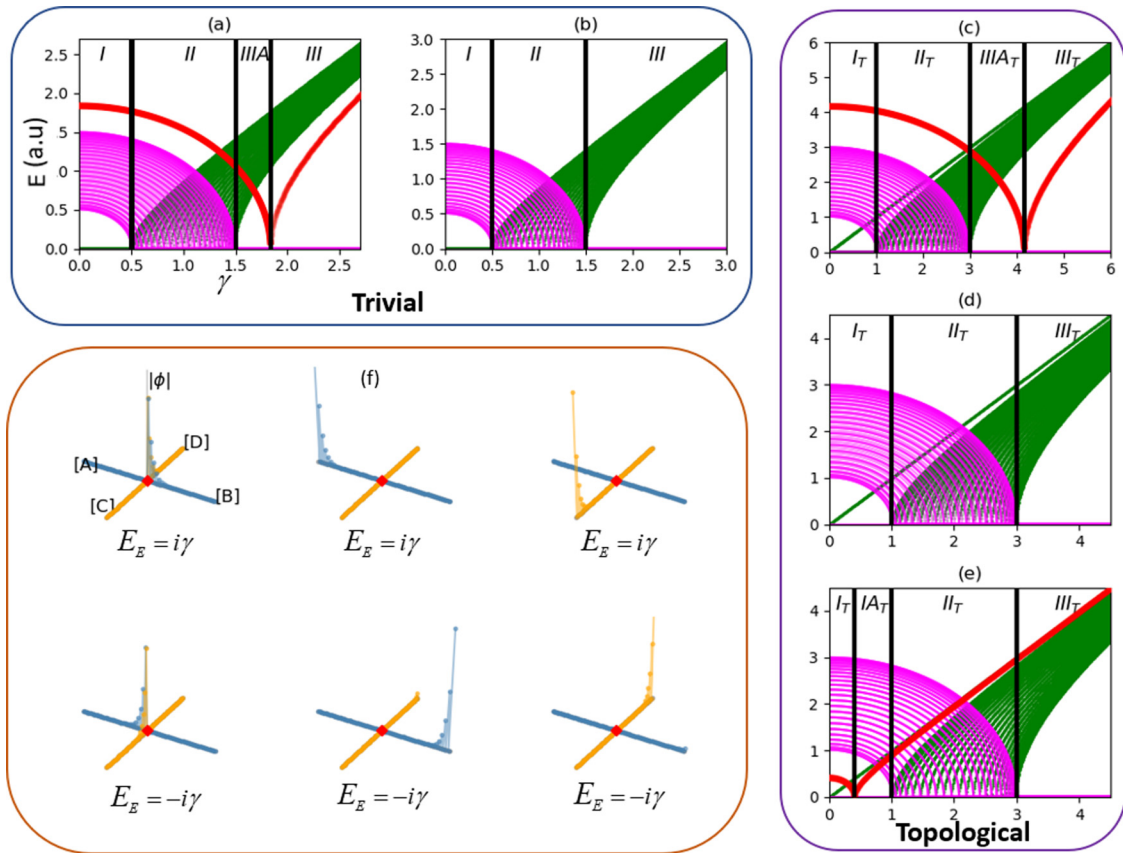


FIG. 6. Phase diagrams for the non-Hermitian crossed-chain system as a function of the gain parameter γ for $M = 50$, for different coupling schemes. Pink and green lines denote the absolute value of the real and imaginary parts, respectively, of the energy pseudospectrum in arbitrary units. Thick red lines denote the isolated localized defect state when it exists. Phase regions are separated by vertical black lines and are denoted by roman numerals. (a) Trivial: $\tilde{a} = 0.5a$, $\Delta = 1.5$. (b) Trivial: $\tilde{a} = 0.5a$, $\Delta = 0.5$. (c) Topological: $\tilde{a} = 2a$, $\Delta = 1$. (d) Topological: $\tilde{a} = 2a$, $\Delta = 0.5$. (e) Topological: $\tilde{a} = 2a$, $\Delta = 0.12$. (f) Amplitudes of the six edge states in the topological regime, $\tilde{a} = 2a$, $\Delta = 1$ and $\gamma = 0.5$. The three states on the top have energies $i\gamma$, and the three states on the bottom have energies $-i\gamma$.

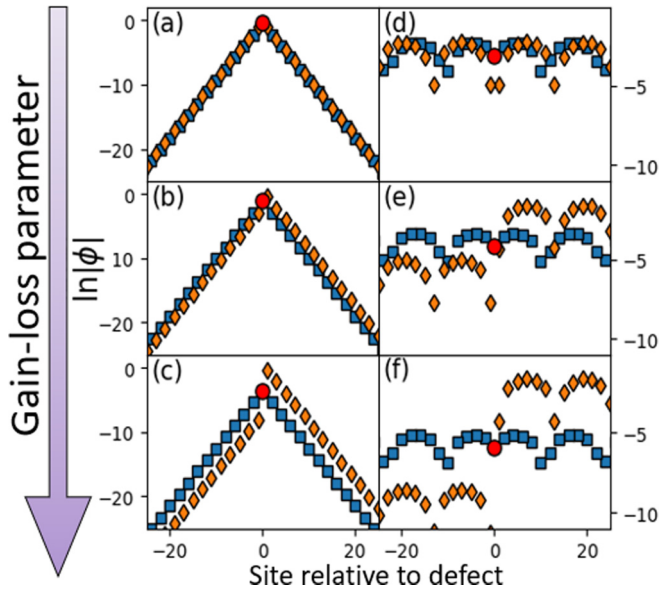


FIG. 7. Amplitude profiles of a localized defect state in the crossed-chain structure along one direction, shown in natural-logarithmic scale, for different values of γ for $\tilde{a} = 2a$, $\Delta = 1$ and $M = 50$. Sites are numbered relative to the defect site. The blue squares (orange diamonds) denote the a, c (b, d) sublattices, and the red circle denotes the defect site. (a) $\gamma < |E_\Delta|$ is the amplitude profile is spatially symmetric around the defect site. For (b) $\gamma > |E_\Delta|$ and (c) $\gamma \gg |E_\Delta|$, the spatial symmetry of the amplitude profile around the defect breaks; however, the localization length remains identical in (a)–(c) for all sublattices. Similarly, for an extended singlet state ($n = 84$), at (d) $\gamma < |E_{84}|$, the amplitude profile is symmetric around the defect. For (e) $\gamma > |E_{84}|$ and (f) $\gamma \gg |E_{84}|$, the spatial symmetry breaks, but the wave number remains unchanged.

When $\Delta^2 < (\tilde{a} - a)/4\tilde{a}$ [Fig. 6(e)], the localized defect states E_Δ are inside the bandgap, meaning that they coalesce in an exceptional point at $|E_\Delta| = \gamma < (a - \tilde{a})^2$. This creates a unique phase diagram, wherein for $|E_\Delta| < \gamma < (a - \tilde{a})^2$, the bulk pseudospectrum is PT symmetric, while the protected edge and localized defect states are PT broken. We denote this phase by IA_T .

It is important to note that PT -symmetry breaking of any pair of singlet states, is associated with a transition in which the spatial symmetries of the singlet-state amplitude profiles break. We have shown in Appendix F that, in the PT -symmetric regime, the amplitude profile of a singlet state is symmetric around the defect site, up to a constant phase shift between the sublattices constituting each SSH chain. This phase shift is equal for one pair of identical chains and has the opposite sign for the complex-conjugate pair of chains (denoted $\{A, C\}$ and $\{B, D\}$, respectively, in Fig. 4). When crossing the exceptional point into the PT -broken regime, two amplitude profiles are obtained, one for every pair of SSH chains. The sublattice amplitudes in different chain pairs are related to one another, and in fact, each of the two sublattices in every SSH chain exhibits different amplitudes but identical wave numbers with respect to the other sublattice, as shown qualitatively in Fig. 7. This transition was not discussed in previous works in the context of bulk states because the division of bulk states into $K - 1$ -degenerate

and spatially symmetric singlet manifolds is manifested clearly only when a higher-dimensional system with $K > 2$ is considered.

We also argue that the non-Hermitian crossed-chain structure illustrated in Fig. 4 is a generalization of the non-Hermitian PT -symmetric 1D structure considered in, e.g., Ref. [16]. This statement is not trivial since the crossed-chain description as two coupled SSH pairs is ambiguous. However, the phase transition mentioned above for the higher-dimensionality crossed-chain structure also occurs in the 1D case, as shown in Appendix F. This resemblance demonstrates that coupling two 1D P - and T - (but not PT -) symmetric systems at their center that forms the non-Hermitian crossed-chain system results in a system exhibiting the behavior of the 1D T - and PT - (but not P -) symmetric configuration.

V. CONCLUSIONS

Defect-induced effects on lattices in more than 1D have been generally overlooked in the recent spur of research pertaining to topological photonics. In this paper, we have performed a comprehensive analysis of a crossed-chain system, comprised of four identical 1D SSH lattices, coupled at a single point through a mutual site acting as a defect. We have investigated a topological structure that consists of several SSH chains coupled at a single site with dimension higher than one.

The manifestation of higher dimensionality at the mutual defect site introduces a type of localized defect state that does not exist for a basic defect in the topologically trivial 1D crossed-chain scheme. Moreover, the higher dimensionality is one of the parameters that leads to a distinction between the localization lengths of the localized zero-energy state and the defect states in the topologically nontrivial regime.

An important result of this paper is that a Hermitian crossed-chain system consisting of K SSH chains can be decomposed into a reduced representation of $K - 1$ identical disconnected SSH chains, described by a $K - 1$ -degenerate manifold, and a single SSH chain connected via a nonreciprocal coupling to an external reservoir, described by a separate singlet manifold. The former manifold is comprised of states that are superpositions of eigenstates of individual SSH chains (including topological edge states for the topological regime). The latter manifold has spatially symmetric states and a nonzero defect-site amplitude and includes the localized-defect states. Interestingly, the system describing the SSH chain coupled to an effective reservoir is non-Hermitian. However, both representations of the system are isospectral and so are equivalent.

Our rigorous analysis yields an exact calculation of the energies and wave numbers of the entire pseudospectrum of the crossed-chain structure as a function of the internal SSH coupling coefficients as well as the defect coupling strengths. The theory developed here predicts the existence of localized defect states that are isolated from the bulk pseudospectrum and thus robust; furthermore, the energies of these localized states can be tuned by changing the defect coupling strength and can be placed outside of the bulk, within the energy bandgap, or merged into the bulk states altogether.

These results also apply when non-Hermiticity in the form of alternating onsite gain and loss is introduced to the system. For a system comprised of two pairs of SSH chains, as illustrated in Fig. 4, the reduced representation is justified also for the non-Hermitian case. Furthermore, our analysis yielded that the wave numbers of the nonzero states in the system are not affected by the non-Hermiticity.

Constructing phase diagrams of the crossed-chain system under varying gain-loss parameters for different topologies and defect coupling strengths, we demonstrated distinctive PT -symmetry regimes for various cases. Some of these phase diagrams have no parallels in 1D with a basic defect and result from the higher dimensionality of our proposed structure.

An important contribution is the demonstration of spatial symmetry breaking of the amplitude profile for the singlet states of the system at exceptional points, not only for localized states but also for bulk states. Although this effect was encountered previously for localized defect states in the 1D case, due to our analysis of the spatially symmetric nature of the singlet states (that is manifested in higher dimensions), this was proven also for bulk states.

The crossed-chain structure has a potential impact on realizations of coherent arrays of lasers since it can be used as a building block for a full 2D networked structure with topologically protected lasing sites distributed over the entire 2D area, localized on defects rather than the existing proposals of topological coherent lasing only on the 1D interface between 2D topological structures. This paper is also of high relevance for other applications of topological phases, including the study of polymer chains (that was the original seed of the SSH model), where the polymer chains are cross-linked, which is a very typical structure in polymer science.

APPENDIX A

We restate the Hamiltonian in Eq. (3) cf. Eq. (4) in an explicit form for an isotropic crossed-chain configuration (i.e., $M_\sigma = M$, $a_\sigma = a$, $\tilde{a}_\sigma = \tilde{a}$, $\Delta_\sigma = \Delta$). For completeness, we will work in the general case of K identical SSH chains coupled at the defect element. Defining $\psi_n^a = \phi_j$, $j = 2n-1$ and $\psi_n^b = \phi_j$, $j = 2n$ for $1 \leq n < M/2$,

$$E_\Delta \psi_n^a = a\psi_n^b + \tilde{a}\psi_{n-1}^b, \quad (\text{A1})$$

$$E_\Delta \psi_n^b = a\psi_n^a + \tilde{a}\psi_{n+1}^a, \quad (\text{A2})$$

where E_Δ denotes the defect state energy. Applying the ansatz $\psi_{n-1}^{a/b} = \psi_n^{a/b}\lambda$ for $\lambda = e^{-\kappa}$, $\kappa \in \mathbb{R}^+$ such that $|\lambda| < 1$, Eq. (A1) yields

$$\frac{\psi_n^a}{\psi_n^b} = \frac{a + \tilde{a}\lambda}{E_\Delta}, \quad n < \frac{M}{2}, \quad (\text{A3})$$

while plugging Eq. (A2) into Eq. (A1) recovers Eq. (5):

$$E_\Delta^2 = a^2 + \tilde{a}^2 \pm 2a\tilde{a} \cosh \kappa. \quad (\text{A4})$$

The localization length zero-energy state E_0 is obtained if the LHS of Eq. (A4) is set to zero and κ is replaced by η_0 (with a minus sign before the hyperbolic cosine so that the LHS vanishes), in agreement with the literature for the 1D problem, e.g., Refs. [12,52].

Note that Eq. (5) considers only the plus sign in Eq. (A4) due to the consideration of $\Delta = 1$. For the case $n = M/2$,

$$E_\Delta \psi_{M/2}^b = a\psi_{M/2}^a + \Delta \tilde{a}\psi_\Delta, \quad (\text{A5})$$

where ψ_Δ denotes the amplitude of the defect state, and

$$E_\Delta \psi_\Delta = K\tilde{a}\Delta\psi_{M/2}^b. \quad (\text{A6})$$

Substituting Eq. (A5) into Eq. (A6) gives us

$$\frac{\psi_M^a}{\psi_M^b} = \frac{1}{a} \left[E_\Delta - \frac{K(\tilde{a}\Delta)^2}{E_\Delta} \right]. \quad (\text{A7})$$

Applying the ansatz to Eq. (A7) and using Eq. (A3), one arrives at

$$\lambda = \frac{E_\Delta^2 - K(\tilde{a}\Delta)^2 - a^2}{a\tilde{a}}, \quad (\text{A8})$$

which reaffirms our choice of $\lambda \in \mathbb{R}$. Finally, from plugging the expression for the energy of the defect state Eq. (A4) into Eq. (A8), we arrive at

$$\Delta^2 = \frac{\tilde{a} + a\lambda(s)^{-1}}{K\tilde{a}}, \quad (\text{A9})$$

where $\lambda(s) = e^{is}$, and $s = i\kappa$ if the localized defect-state energy lies outside the bulk pseudospectrum, or $s = \pi + i\kappa$ if E_Δ lies within the gap. By substituting $\Delta = 1$ in Eq. (A9), Eq. (6) from the main text is obtained. Plugging this in back into Eq. (A8),

$$E_\Delta^2 = a^2 + \tilde{a}^2 + \left[\frac{a^2 + (K\Delta^2 - 1)^2\tilde{a}^2}{K\Delta^2 - 1} \right], \quad (\text{A10})$$

and comparing this to the SSH bulk state expression $E^2(k) = a^2 + \tilde{a}^2 + 2a\tilde{a} \cos k$, we surmise that nonbandgap isolated defect states exist for Δ , satisfying

$$\left| \frac{a^2 + (K\Delta^2 - 1)^2\tilde{a}^2}{K\Delta^2 - 1} \right| > 2a\tilde{a} + \varepsilon, \quad (\text{A11})$$

where the term ε stems from the finiteness of the lattice, as the true distribution of the localized states deviates from the ansatz for a finite number of elements. We shall omit ε in our calculations, as this term is negligible for lattices on the order of tens of elements, which we consider in this paper. Equation (A11) restates Eq. (A9) under the ansatz of exponential decay and the long-chain approximation:

$$\Delta^2 > \frac{a + \tilde{a}}{K\tilde{a}}, \quad (\text{A12})$$

for the positive branch of Eq. (A11), or

$$\Delta^2 < \frac{-a + \tilde{a}}{K\tilde{a}}, \quad (\text{A13})$$

for its negative branch, implying $\lambda(\kappa) \rightarrow \lambda(\kappa - i\pi)$ and leading to the restatement of the localized defect state energy as

$$E_\Delta^2 = a^2 + \tilde{a}^2 - 2a\tilde{a} \cosh \kappa, \quad \Delta^2 < \frac{\tilde{a} - a}{K\tilde{a}} \quad \text{ingap}, \quad (\text{A14})$$

$$E_\Delta^2 = a^2 + \tilde{a}^2 + 2a\tilde{a} \cosh \kappa, \quad \Delta^2 > \frac{a + \tilde{a}}{K\tilde{a}} \quad \text{outsidegap}, \quad (\text{A15})$$

with $2a\tilde{a}\cosh(2\kappa) = [a^2 + (K\Delta^2 - 1)^2\tilde{a}^2]/(K\Delta^2 - 1)$. Note that this expression does not diverge, as Δ^2 is either larger or smaller than $1/K$ when defect states exist since $\{a, \tilde{a}\} \in \mathbb{R}^+$. Additionally, as seen in Eq. (A15), no localized states exist in the topologically trivial case for $\Delta^2 < \frac{-a+\tilde{a}}{K\tilde{a}}$.

APPENDIX B

Our goal in this section is to find relations between the energies, wave numbers, and defect coupling strength for the bulk states. We will restrict this calculation to the case of $K = 4$ SSH chains, although generalization to any number can be easily obtained.

Firstly, we formulate an analytical relation between the lattice site amplitudes in the bulk pseudospectrum of states. For a single SSH chain comprised of $M/2$ unit cells with open boundary conditions, the bulk states will have the general form of sine functions, with wave numbers k_m quantized for each of the M ($M-2$) bulk states of the trivial (topological) configuration, given by the solution to the eigenvalue problem of the Hamiltonian of the system. More specifically, the boundary conditions of the SSH chain read $\psi_0^b = 0$, $\psi_{M/2+1}^a = 0$, which can be restated for the m th state for the b sublattice as the ansatz:

$$\frac{\psi_{n,m}^b}{\sin(k_m n)} = C_m, \quad (\text{B1})$$

for $n \in \{1 \dots M/2\}$ and some constant C_m . Defining

$$\chi_{n,m} \equiv \frac{\sin[k_m(n-1)]}{\sin(k_m n)}, \quad (\text{B2})$$

and substituting Eq. (B1) in Eqs. (A1) and (A2) would yield the relations:

$$\frac{\psi_{n,m}^a}{\psi_{n,m}^b} = \frac{a + \tilde{a}\chi_{n,m}}{E_m}, \quad (\text{B3})$$

$$\frac{\psi_{n+1,m}^a}{\psi_{n,m}^b} = \frac{\frac{a}{\chi_{n+1,m}} + \tilde{a}}{E_m}, \quad (\text{B4})$$

for $\forall n: k_m n \neq 0$. Substituting these back in Eq. (A2) for $n < M/2$ and applying the trigonometric relation $\chi_{n,x} + \chi_{n+1,x}^{-1} = 2 \cos x$ yields the known bulk SSH dispersion relation $E^2(k_m) = a^2 + \tilde{a}^2 + 2a\tilde{a}\cos k_m$. Note that this expression does not depend on n . Solving for $n = M/2$ and applying the boundary condition $\psi_{M/2+1}^a = 0$ yields the implicit equation for k_m :

$$E_T^2(k_m) = a^2 + a\tilde{a}\chi_{M/2,m}, \quad (\text{B5})$$

the solutions of which yield the supported wave numbers for the triplet pseudospectrum.

Secondly, as discussed in the main text, we treat the system as comprised of four degenerate SSH chains connected to an external system with coupling strength $\Delta\tilde{a}$. However, to maintain an identical amplitude profile of the degenerate chains to these in the crossed-chain configuration, we assume that the external system experiences a coupling strength of $4\Delta\tilde{a}$.

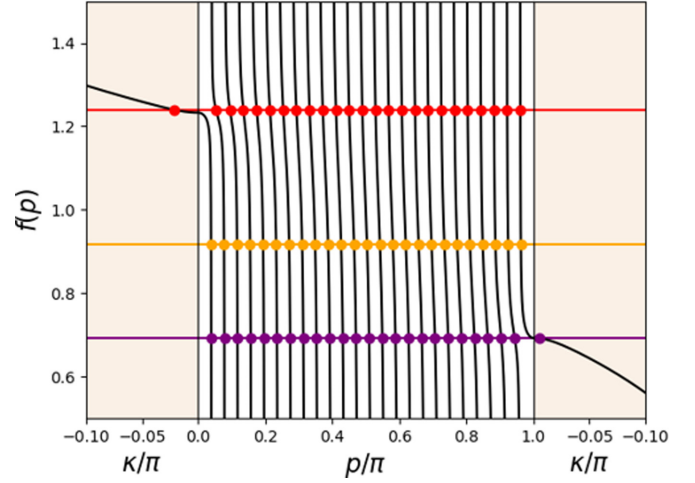


FIG. 8. Numerical calculation of $f(p)$ for $\tilde{a} = 2a$ with $M = 50$. Solutions $p_n(\Delta)$ are the intersections $f(p) = 2\Delta$ marked by full circles. Only $\text{Re}(p) \geq 0$ solutions are presented. The graph is analytically continued for complex wave numbers $p = i\kappa$ and $p = \pi + i\kappa$ on the left and right panels, respectively, wherein the solutions describe localized states. Red circles (top): $\Delta = \sqrt{(a + \tilde{a})/4\tilde{a}} + 7.5 \times 10^{-3}$ with 24 extended and one nonmidgap solutions (defect states are excluded from the bulk and are localized); orange circles (middle): $\Delta = 0.75\sqrt{(a + \tilde{a})/4\tilde{a}}$ with 25 extended solutions (defect states are merged into the bulk); purple circles (bottom): $\Delta = \sqrt{(\tilde{a} - a)/4\tilde{a}} - 7.5 \times 10^{-3}$ with 24 extended and one localized in-gap solutions (defect states are excluded from the bulk and are localized).

We write the equations for the defect and the $n = M/2$ cell

$$E_S(p)\psi_{M/2,p}^b = \Delta\tilde{a}\psi_{\Delta,p} + a\psi_{M/2,p}^a, \quad (\text{B6})$$

$$E_S(p)\psi_{M/2,p}^a = a\psi_{M/2,p}^b + \tilde{a}\psi_{M/2-1,p}^b, \quad (\text{B7})$$

$$E_S(p)\psi_{\Delta,p} = 4\Delta\tilde{a}\psi_{M/2,p}^b. \quad (\text{B8})$$

The S subscript for the energy denotes the energy of the singlet state with the shifted wave number $p = k_m + \delta k_m$. Plugging Eqs. (B8) and (B7) into Eq. (B6) for $E_S(p) \neq 0$ yields

$$E_S^2(p) = a^2 + a\tilde{a}\chi_{M/2,p} + 4(\Delta\tilde{a})^2, \quad (\text{B9})$$

which is equivalent to Eq. (B5) when $\Delta = 0$. Substituting the SSH dispersion relation $E^2(p)$ for the shifted wave numbers $p = k_m + \delta k_m$ in Eq. (B9) and reformulating to the implicit form $f(p) = 2\Delta$, we obtain

$$f(p) = \sqrt{1 + \frac{a}{\tilde{a}} \left[\cos(p) + \cot\left(\frac{pM}{2}\right) \sin(p) \right]}. \quad (\text{B10})$$

Considering $\Delta > 0$, solving $f(p) = 2\Delta$ to recover the wave numbers for a given value of Δ , and substituting the numerically obtained results in the SSH dispersion relation, we recover the eigenvalues of the shifted states obtained from Eq. (3) (Fig. 8). Note that, to obtain the complex wave number of the localized states, one must substitute $p = i\kappa$ for $\Delta^2 > (a + \tilde{a})/4\tilde{a}$ or $p = \pi + i\kappa$ for $\Delta^2 < (\tilde{a} - a)/4\tilde{a}$ in Eq. (B10).

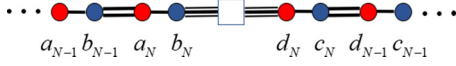


FIG. 9. Schematic of one axis of the complex Su-Schrieffer-Heeger (SSH) crossed-chain configuration. The white square denotes the defect site, red circles denote gain γ , blue circles denote loss $-\gamma$, black line denotes a coupling strength a , double line denotes a coupling strength \tilde{a} , and finally, triple line denotes the defect coupling strength $\tilde{a}\Delta$.

The wave number shifts δk_m for the bulk states could be numerically obtained from

$$\delta k_m(\Delta) = p_m(\Delta) - k_m, \quad (\text{B11})$$

where $p_m(\Delta)$ is the m th element of the ordinal sequence defined by $p(\Delta) \equiv \{p : f(p) = 2\Delta\}$ and $k_m = p_m(0)$. It can be deduced from the cotangent function in Eq. (B10) and also obtained numerically, as demonstrated in Fig. 8, that $\max_{\Delta} |\delta k_m(\Delta)| < |k_m - k_{m+1}|$, so that the shifted singlet energies separate inhomogeneously from the triplet pseudospectrum at $\Delta > 0$ but never exceed the energy level of the next degenerate triplet; taking $\Delta \rightarrow \infty$ in $f(p) = 2\Delta$ necessitates $\cot(p_m M) \rightarrow \infty$, so that $p_m(\Delta \gg 1) \rightarrow \pm m\pi/M$ for $m \in \{1 \dots M/2 - 1\}$.

APPENDIX C

Using the same notations as in Appendix A, we start in a similar manner; however, the introduction of the gain parameter under PT symmetry divides the four chains into two pairs—one pair of chains with the loss site adjacent to the defect and one pair with the gain site adjacent to it (Fig. 9). We will focus on the crossed-chain case ($K = 4$). Generalizations of these calculations can be done for an even number of SSH chains, as our assumptions rely on PT symmetry in the system. Without loss of generality,

$$(E_{\Delta,\gamma} - i\gamma)\psi_n^a = a\psi_n^b + \tilde{a}\psi_{n-1}^b, \quad (\text{C1})$$

$$(E_{\Delta,\gamma} + i\gamma)\psi_n^b = a\psi_n^a + \tilde{a}\psi_{n+1}^a, \quad (\text{C2})$$

for the first pair of chains, and

$$(E_{\Delta,\gamma} + i\gamma)\psi_n^c = a\psi_n^d + \tilde{a}\psi_{n-1}^d, \quad (\text{C3})$$

$$(E_{\Delta,\gamma} - i\gamma)\psi_n^d = a\psi_n^c + \tilde{a}\psi_{n+1}^c, \quad (\text{C4})$$

for the second, for $n < M/2$.

Assuming again that $\psi_{n-1}^x = \psi_n^x \lambda$, with $x \in \{a, b, c, d\}$, $\lambda = |\lambda|e^{i\varphi}$, $|\lambda| < 1$, and some phase $\varphi \in \mathbb{R}$ for the localized nonmidgap defect state, plugging Eq. (C2) into Eq. (C1) recovers

$$E_{\Delta,\gamma}^2 = a^2 + \tilde{a}^2 + a\tilde{a}(\lambda + \lambda^{-1}) - \gamma^2, \quad (\text{C5})$$

which suggests that $E_{\Delta,\gamma}$ is either a purely real or a purely imaginary quantity, depending on the magnitude of γ . Replacing $\lambda = e^{-\kappa}$ or $\lambda = e^{i\pi - \kappa}$ restores Eq. (15) or (16), respectively. We shall first consider $E_{\Delta,\gamma} \in \mathbb{R}$. Since applying the complex conjugate operator to Eqs. (C3) and (C4) yields

Eqs. (C1) and (C2), respectively, it is clear that $\psi_n^a = \psi_n^{c*}$ and $\psi_n^b = \psi_n^{d*}$, so that Eqs. (C4) and (C3) become redundant. We write the equation for the defect site:

$$E_{\Delta,\gamma}\psi_{M/2} = 2\tilde{a}\Delta\psi_{M/2}^b + 2\tilde{a}\Delta\psi_{M/2}^{b*}, \quad (\text{C6})$$

and apply the ansatz, and since $\psi_{M/2} \in \mathbb{R}$, we can conclude that $\varphi = 0$, and so $\lambda \in \mathbb{R}$. We extract from Eq. (C1) the relation:

$$\frac{\psi_n^a}{\psi_n^b} = E_{\Delta,\gamma} \frac{a + \tilde{a}\lambda}{E_{\Delta,\gamma}^2 + \gamma^2} + i\gamma \frac{a + \tilde{a}\lambda}{E_{\Delta,\gamma}^2 + \gamma^2}, \quad (\text{C7})$$

for $n < M/2$, from which we obtain

$$\text{Im}\psi_n^a = \frac{a + \tilde{a}\lambda}{E_{\Delta,\gamma}^2 + \gamma^2} (E_{\Delta}\text{Im}\psi_n^b + \gamma\text{Re}\psi_n^b), \quad (\text{C8})$$

$$\text{Re}\psi_n^a = \frac{a + \tilde{a}\lambda}{E_{\Delta,\gamma}^2 + \gamma^2} (E_{\Delta}\text{Re}\psi_n^b - \gamma\text{Im}\psi_n^b). \quad (\text{C9})$$

For $n = M/2$, we write

$$(E_{\Delta,\gamma} + i\gamma)\psi_{M/2}^b = a\psi_{M/2}^a + \Delta\tilde{a}\psi_{M/2}. \quad (\text{C10})$$

Solving separately for the real and imaginary parts of Eq. (C10),

$$E_{\Delta,\gamma}\text{Re}\psi_{M/2}^b - \gamma\text{Im}\psi_{M/2}^b = a\text{Re}\psi_{M/2}^a + \Delta\tilde{a}\text{Re}\psi_{M/2}, \quad (\text{C11})$$

$$E_{\Delta,\gamma}\text{Im}\psi_{M/2}^b + \gamma\text{Re}\psi_{M/2}^b = a\text{Im}\psi_{M/2}^a + \Delta\tilde{a}\text{Im}\psi_{M/2}. \quad (\text{C12})$$

Since $\text{Im}\psi_{M/2} = 0$, multiplying Eq. (C12) by $\lambda^{M/2-n}$ and plugging the result into Eq. (C8) yields

$$\text{Im}\psi_n^a = \frac{a + \tilde{a}\lambda}{E_{\Delta,\gamma}^2 + \gamma^2} (a\text{Im}\psi_n^a), \quad (\text{C13})$$

which for $\tilde{a} \neq 0$ can be true if and only if $\forall n : \text{Im}\psi_n^a \equiv 0$. Taking Eqs. (C11) and (C12) cf. Eq. (C6),

$$\frac{\psi_{M/2}^b}{\psi_{M/2}^a} = a \frac{E_{\Delta,\gamma} + i\gamma}{E_{\Delta,\gamma}^2 + \gamma^2 - 4(\tilde{a}\Delta)^2}. \quad (\text{C14})$$

Comparing this with Eq. (C7) results in

$$\lambda = \frac{E_{\Delta,\gamma}^2 + \gamma^2 - 4(\tilde{a}\Delta)^2 - a^2}{a\tilde{a}}, \quad (\text{C15})$$

and using Eq. (C5), one has

$$\Delta^2 = \frac{\tilde{a} + a\lambda^{-1}}{4\tilde{a}}. \quad (\text{C16})$$

This reproduces Eq. (10) from the main text, suggesting that the defect state remains unaffected by the introduction of onsite non-Hermiticity in the considered scheme, while $E_{\Delta,\gamma} \in \mathbb{R}$. Furthermore, the nonmidgap defect state energies in Eq. (C5) can be re-expressed to yield a generalization of Eq. (A10):

$$E_{\Delta,\gamma}^2 = a^2 + \tilde{a}^2 + \left[\frac{a^2 + (4\Delta^2 - 1)^2 \tilde{a}^2}{4\Delta^2 - 1} \right] - \gamma^2. \quad (\text{C17})$$

A transition of the system occurs at the PT -symmetry breaking point $E_{\Delta,\gamma}^2 = 0$, beyond which point $E_{\Delta,\gamma}$ becomes purely imaginary, and therefore, the relations between Eqs. (C1) and (C2) to Eqs. (C3) and (C4) no longer imply that the two chain pairs defined by their lattice sites $\{a, b\}$ and

$\{c, d\}$, respectively, are complex conjugates. Thus, we must assume two dissimilar pairs of complex SSH chains. Denoting $E_{\Delta, \gamma} = iW$ with $W \in \mathbb{R}$ for convenience, we have

$$iW \psi_{\Delta} = 2\tilde{a}\Delta \psi_{M/2}^b + 2\tilde{a}\Delta \psi_{M/2}^d, \quad (\text{C18})$$

$$i(W - \gamma_{\mu})\psi_{M/2}^{\mu} = a\psi_{M/2}^{\nu} + \tilde{a}\Delta \psi_{\Delta}, \quad (\text{C19})$$

where we have defined $\mu \in \{b, d\}$ and $\nu \in \{a, c\}$ such that the pair $(\mu, \nu) \in \{(b, a), (d, c)\}$. Additionally, $\gamma_b = -\gamma_a = -\gamma$. We keep the assumption of a localized state, wherein the localization length remains dependent only on the coupling coefficients of the structure. To justify this for dissimilar chains, we denote the evanescence factors λ_{ab} and λ_{cd} , and plug Eq. (C2) into Eq. (C1) and Eq. (C4) into Eq. (C3), recovering Eq. (C5), respectively, for $E_{\Delta, \gamma}^2(\lambda_{ab}, \gamma)$ and $E_{\Delta, \gamma}^2(\lambda_{cd}, \gamma)$. Equating these expressions yields a true statement if and only if $\lambda_{ab} = \lambda_{cd}$.

Denoting $\lambda \equiv \lambda_{ab} = \lambda_{cd}$, from Eqs. (C1) and (C3), we obtain

$$\frac{\psi_n^{\nu}}{\psi_n^{\mu}} = -i \frac{a + \tilde{a}\lambda}{W + \gamma_{\mu}}, \quad (\text{C20})$$

for $1 \leq n < M/2$. It is implied from Eq. (C20) that the elements in each unit cell are shifted by a constant phase of $\pi/2$ with respect to one another. Solving Eq. (C19) cf. Eq. (C20) separately for the real and imaginary parts and consolidating the expressions, we arrive at

$$\psi_{M/2}^{\mu} = -i \frac{\tilde{a}\Delta(W + \gamma_{\mu})}{W^2 - \gamma^2 + a^2 + a\tilde{a}\lambda} \psi_{\Delta}. \quad (\text{C21})$$

Plugging these back into Eq. (C19) generalizes Eq. (C20) to $n = M/2$. Finally,

$$\psi_{M/2}^a = \frac{-\tilde{a}\Delta(a + \tilde{a}\lambda)}{W^2 - \gamma^2 + a^2 + a\tilde{a}\lambda} \psi_{\Delta}, \quad (\text{C22})$$

$$\psi_{M/2}^c = \frac{-\tilde{a}\Delta(a + \tilde{a}\lambda)}{W^2 - \gamma^2 + a^2 + a\tilde{a}\lambda} \psi_{\Delta}, \quad (\text{C23})$$

so that

$$\psi_n^a = \psi_n^c, \quad (\text{C24})$$

$$\psi_n^b = \frac{W - \gamma}{W + \gamma} \psi_n^d, \quad (\text{C25})$$

for all n . This result demonstrates a breaking of spatial symmetry in the system that occurs when the state crosses an exceptional point and PT symmetry breaks, while the symmetric intercell exponential decay ansatz (see Fig. 7) is maintained. When the gain parameter is very large, i.e., $\gamma \gg 1$ (so that $\gamma \approx -W$), the site amplitudes of the $\{a, b\}$ chains are held at zero, and the site with the highest amplitude is the $\psi_{M/2}^d$ site, as $|\psi^{\Delta}| \rightarrow 0$. This effectively demonstrates a negligible penetration of energy into the defect and the $\{a, b\}$ chains. From Eqs. (C18) and (C21)–(C23), we recover Eq. (C16), reaffirming that the localization length depends on the defect strength of the structure and not on its gain parameter.

APPENDIX D

We combine the assumptions of Appendixes B and C to analyze the relations between the energies of the bulk states, the defect coupling strength, and the gain parameter.

We start by applying the same ansatz in Eq. (B1) since the addition of a constant imaginary gain (loss) term to every second site should not affect our underlying assumptions, as one can define a complex energy term $\varepsilon_q \equiv E_q + (-i)\gamma$ for the sublattices of the sites adjacent to the defect. Since now we have two types of SSH chains, as illustrated in Fig. 9, we restate the ansatz in Eq. (B1):

$$\frac{\psi_{n,m}^{\mu}}{\sin(k_m n)} = C_m^{\mu}, \quad (\text{D1})$$

with the same (μ, ν) notation of Appendix C. Plugging Eq. (D1) into Eqs. (C1)–(C4), with the bulk state energies denoted $E_{\gamma}(k_m)$ instead of $E_{\Delta, \gamma}$, and the definition in Eq. (B2) yields

$$\frac{\psi_{n,m}^{\nu}}{\psi_{n,m}^{\mu}} = \frac{a + \tilde{a}\chi_{n,m}}{E_{\gamma}(k_m) + i\gamma_{\mu}}, \quad (\text{D2})$$

$$\frac{\psi_{n+1,m}^{\nu}}{\psi_{n,m}^{\mu}} = \frac{\frac{a}{\chi_{n+1,m}} + \tilde{a}}{E_{\gamma}(k_m) - i\gamma_{\mu}}, \quad (\text{D3})$$

for $\forall n < M/2 : k_m n \neq 0$. From substitution of Eqs. (D2) and (D3) in Eq. (C2), we recover the dispersion relation $E_m^2(k_m) = a^2 + \tilde{a}^2 + 2a\tilde{a}\cos k_m - \gamma^2$. The triplet energies $E_{T, \gamma}(k_m)$ are obtained by imposing the boundary condition $\psi_{M/2+1, m}^{\nu} = 0$ in the same manner as in Appendix B, and we get

$$E_{T, \gamma}^2(k_m) + \gamma^2 = a^2 + a\tilde{a}\chi_{M/2, m}. \quad (\text{D4})$$

For the singlet bulk energies $E_{S, \gamma}(p)$, we note that $E_{S, \gamma}(p)$ can be either purely real or purely imaginary. We begin with the case $E_{S, \gamma}(p) \in \mathbb{R}$, for which $\psi_{n,m}^b = \psi_{n,m}^{d*}$ for all n and m . We write the equations for the effective system that describes the singlet states:

$$[E_{S, \gamma}(p) - i\gamma_{\mu}]\psi_{M/2, p}^{\mu} = \Delta\tilde{a}\psi_{\Delta, p} + a\psi_{M/2, p}^{\nu}, \quad (\text{D5})$$

$$E_{S, \gamma}(p)\psi_{\Delta, p} = 4\Delta\tilde{a}\text{Re}\psi_{M/2, p}^{\mu}, \quad (\text{D6})$$

and we solve Eq. (D5) separately for the real and imaginary parts of $\psi_{M/2, p}^{\mu}$. Plugging in Eq. (D6), we obtain for $E_{S, \gamma} \neq 0$:

$$\frac{\psi_{M/2, p}^{\nu}}{\psi_{M/2, p}^{\mu}} = \frac{1}{a} \frac{E_{S, \gamma}^2(p) + \gamma^2 - 4(\tilde{a}\Delta)^2}{E_{S, \gamma}^2(p) + \gamma^2} [E_{S, \gamma}(p) + i\gamma_{\mu}], \quad (\text{D7})$$

which together with Eq. (D2) yields

$$E_{S, \gamma}^2(p) + \gamma^2 = a^2 + \tilde{a}a\chi_{M, q} + 4(\tilde{a}\Delta)^2. \quad (\text{D8})$$

Since in the non-Hermitian case $E_{S, \gamma}^2(p) = a^2 + \tilde{a}^2 + 2a\tilde{a}\cos p - \gamma^2$, this yields exactly Eq. (B9), and so the solution of $f(p) = 2\Delta$ for $\Delta > 0$ and $f(p)$ as defined in Eq. (B10) generates the same solutions $p_m(\Delta)$ as in the Hermitian case. The case of $E_{S, \gamma} = 0$ recovers the E_0 state. Turning to consider $E_q \in i\mathbb{R}$, we define $W(p) \in \mathbb{R}$ through $E_s(p) = iW(p)$ and rewrite the equation for the defect site:

$$iW(p)\psi_{\Delta, p} = 2\Delta\tilde{a}\psi_{M/2, p}^b + 2\Delta\tilde{a}\psi_{M/2, p}^d. \quad (\text{D9})$$

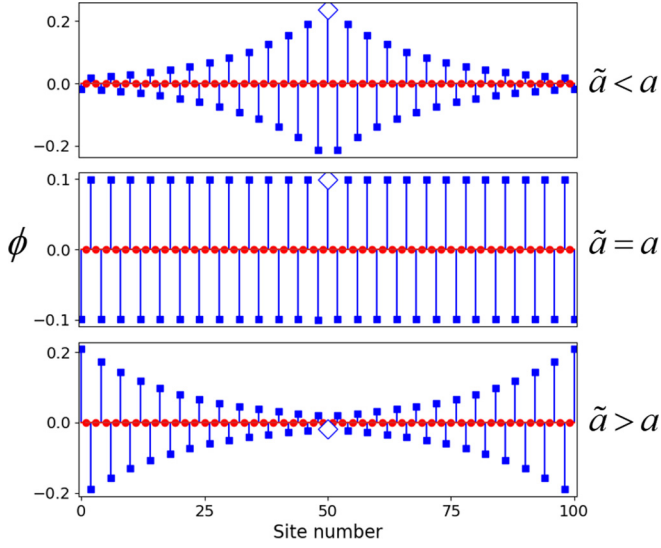


FIG. 10. Zero-energy state of a one-dimensional (1D) crossed chain for trivial Su-Schrieffer-Heeger (SSH) (top), transition point SSH (mid), and topological SSH (bottom) lattices of length $M = 50$. Blue squares indicate sublattice A, red circles indicate sublattice B, and the blue diamond indicates the defect site.

Solving Eq. (D5) for its real and imaginary parts along with Eq. (D2) once for $\{a, b\}$ and once for $\{c, d\}$ results in

$$\frac{\psi_{M/2,p}^\mu}{\psi_{\Delta,p}^\mu} = -i \frac{\tilde{a}\Delta[W(p) + \gamma_\mu]}{W^2(p) - \gamma^2 + a^2 + a\tilde{a}\chi_{M/2,p}}, \quad (\text{D10})$$

implying from Eq. (D2) that, as in the case of localized defect states, when $E_s(p) \in i\mathbb{R}$ —although the two SSH pair amplitude profiles are not spatially symmetric around the defect as in the Hermitian case— $\psi_{n,p}^c = \psi_{n,p}^a$ for all n and p . In fact, it can be readily obtained that Eqs. (C22)–(C25) apply here under the replacement of λ with $\chi_{M/2,p}$ and adequate notations.

Combining Eqs. (D9) and (D10) results in

$$W^2(p) + \gamma^2 = a^2 + a\tilde{a}\chi_{M/2,p} + 4(\tilde{a}\Delta)^2, \quad (\text{D11})$$

which again yields the exact expression in Eq. (B9), for $E_s^2(p) < 0$. Therefore, we conclude that the solution for the wave number equation is not affected by the introduction of non-Hermiticity in the scheme suggested in this paper and that the relation between the defect coupling strength and the shifts in wave numbers is constant for all γ .

APPENDIX E

In this appendix, we will succinctly establish several properties of the localized states of 1D crossed-chain system in the topological regime, with a basic defect ($\Delta = 1$), since this case was not thoroughly addressed in literature.

First, we will demonstrate the phase transition that the zero state E_0 undergoes between the trivial and topological regimes. In Fig. 10, we show the amplitude profile of a 1D crossed-chain system in the trivial and topological regimes as well as in the singular transition point $\tilde{a} = a$. In the trivial regime (stronger intercoupling), only the defect and the A sublattices have nonzero amplitudes, and the amplitude pro-

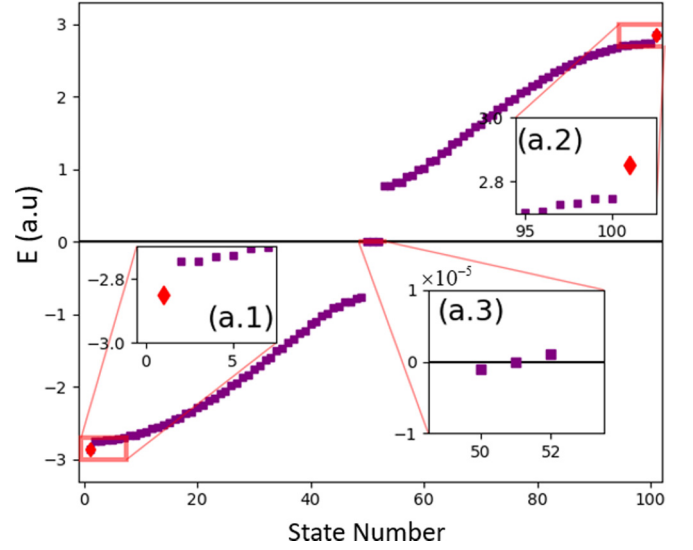


FIG. 11. Pseudospectrum of the one-dimensional (1D) Su-Schrieffer-Heeger (SSH) crossed chain in the topological regime, with $\tilde{a} = 1.75a$ and $M = 50$. Insets (a.1) and (a.2) depict the localized defect states E_Δ (red diamonds), and inset (a.3) depicts the zero-energy state E_0 at the center and the two topological SSH edge states around it. The scale of the energy axis in inset (a.3) demonstrates the precision of the long-chain approximation for the considered system parameters.

file is exponentially decreasing from the defect site. As \tilde{a} increases in the trivial regime, the bandgap shrinks, and the localization length increases until the gap closes at $\tilde{a} = a$ and the zero-energy state E_0 becomes delocalized. When $\tilde{a} > a$, the gap reopens in the topological regime, and the localization shifts to the outer edges of the A sublattices, as now the intercoupling is stronger, and so the defect is strongly coupled to its neighboring sites, so the state diffuses from it rather than centers around it. The amplitudes of the B lattice remain pinned at zero, as can be seen from the Hamiltonian equations of the system for $E = 0$ when a nonzero amplitude at the A lattice is assumed.

The localization length in the topological region is then given by $\eta_0^{\text{topo}} = -\ln(a/\tilde{a})$, and so the general expression of the localization length of E_0 is

$$\eta_0 = \left| \ln \left(\frac{a}{\tilde{a}} \right) \right|. \quad (\text{E1})$$

The pseudospectrum of the system is illustrated in Fig. 11 for the parameters $\tilde{a} = 1.75a$ and $M = 50$. The red diamonds in the insets of Fig. 11(a.1) and 11(a.2) depict the edge states $\pm E_\Delta$, whose properties can be calculated from Appendix A for a basic defect and $K = 2$ in the long-lattice approximation:

$$E_\Delta^2 = a^2 + \tilde{a}^2 + 2a\tilde{a} \cosh \kappa, \quad (\text{E2})$$

$$\kappa = -\ln \left(\frac{a}{\tilde{a}} \right). \quad (\text{E3})$$

The three states in the inset of Fig. 11(a.3) are the zero-energy state E_0 in the center, and two topological SSH edge states E_E on each site. The energies and localization lengths

of these states are known [74], and in the long-lattice approximation are

$$E_E \approx 0, \quad (\text{E4})$$

which is true if and only if

$$\eta_E \approx -\ln\left(\frac{a}{\tilde{a}}\right). \quad (\text{E5})$$

The long-lattice approximation can be justified for our parameters, as seen in Fig. 11(a.3), wherein the scale of the energy axis demonstrates the proximity of E_E to zero.

APPENDIX F

We briefly present an explanation for the behavior of the amplitude profile of a non-Hermitian crossed SSH system with an even number of chains, in the PT -symmetry-preserved and broken regimes to support our claim in the main text. This explanation is also valid for a 1D crossed chain.

While PT symmetry is maintained, only the relative phases between the sublattices of each SSH chain depend on γ , while the amplitude ratio remains constant. Equations (C7) and (D2) that describe the intracell amplitude ratios have the general form:

$$\frac{\psi_{n,m}^{a/c}}{\psi_{n,m}^{b/d}} = \frac{a + \tilde{a}z}{E(\gamma) \pm i\gamma} \equiv \frac{q}{g(\gamma)}, \quad (\text{F1})$$

with $z \in \mathbb{R}$ taking the role of the intercell amplitude ratio λ or $\chi_{m,n}$ for a localized or extended state, respectively. The above is true for a system being comprised of SSH chains and their complex conjugates, thus consisting of four sublattices denoted $\{a, b, c, d\}$, and therefore can be also applied to the 1D case. The plus or minus sign depends on by whether the sublattice a/c has onsite gain or loss, respectively. Considering the dependence of $E(\gamma)$ on γ , Eq. (F1) has a real numerator that does not depend on γ and a complex denominator of the form $g(\gamma) = [C^2 - \gamma^2]^{1/2} \pm i\gamma$, $C \in \mathbb{R}^+$. While $|\gamma| \leq C$,

$$|g(\gamma)| = C, \quad \angle g(\gamma) = \pm \arctan\left[\frac{\gamma}{(C^2 - \gamma^2)^{1/2}}\right], \quad (\text{F2})$$

whereas for $|\gamma| > C$,

$$|g(\gamma)| = |\gamma^2 - C^2|^{1/2} \pm \gamma, \quad \angle g(\gamma) = \pm \frac{\pi}{2}. \quad (\text{F3})$$

Equation (F2) shows that, in the PT -symmetric regime, $|\angle g(\gamma)|$ monotonically increases from 0 for $\gamma = 0$ to $\pi/2$ at $|\gamma| = C$. When the PT symmetry is broken [Eq. (F3)], the sublattices maintain a constant relative $\pi/2$ phase, while their amplitude ratio changes since, in this region, $|g(\gamma)|$ changes monotonically with γ [depending on the sign $\text{Im}g(\gamma)$], while its phase remains constant. This demonstrates the separation of the amplitudes of the sublattices in a single SSH chain when PT symmetry breaks. When two mirrored SSH lattices are coupled, as in Fig. 9, such that the imaginary onsite potentials of the sublattices adjacent to the defect have opposite signs, the sublattice amplitudes ratios in each chain are described by Eq. (F3) with opposing signs. This proves that the amplitude symmetry of the non-Hermitian crossed-SSH system breaks

when PT symmetry is broken, for 1D as well as for higher dimension crossed-chain systems, with the gain-loss scheme considered in this paper.

APPENDIX G

As an indication for the topological phase in the non-Hermitian regime, we numerically demonstrate the robustness of the topological states of the system against structural disorder, following Refs. [13,16] and others.

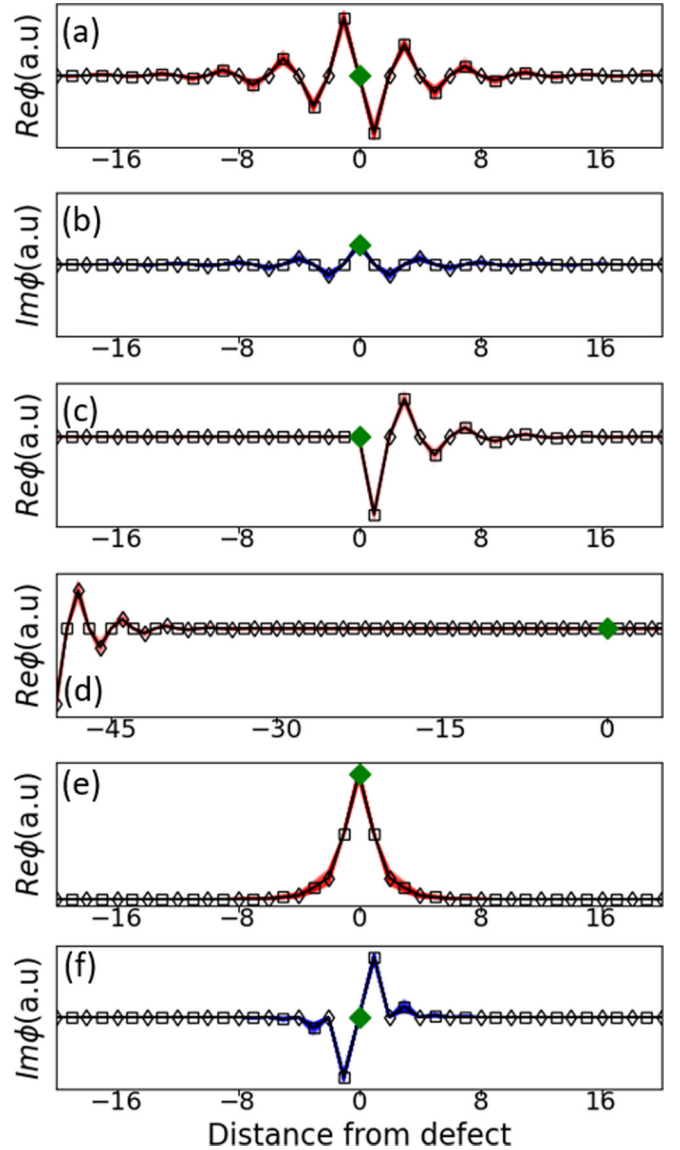


FIG. 12. Amplitude profiles of localized states in a non-Hermitian crossed-chain Su-Schrieffer-Heeger (SSH) structure with $\gamma = 0.5$, $\tilde{a} = 2a$, and $M = 50$ along a single axis. Hollow diamonds mark sublattice A/C, and hollow squares mark sublattice B/D. Full green diamond marks the defect site amplitude. Each subfigure portrays 300 realizations of random disorder with $S = 0.5$ in red (real) or blue (imaginary) lines. Black lines denote the average amplitude profile. (a) Real and (b) imaginary part of the zero state. (c) Inner and (d) outer edge states. (e) Real and (f) imaginary parts of a localized defect state.

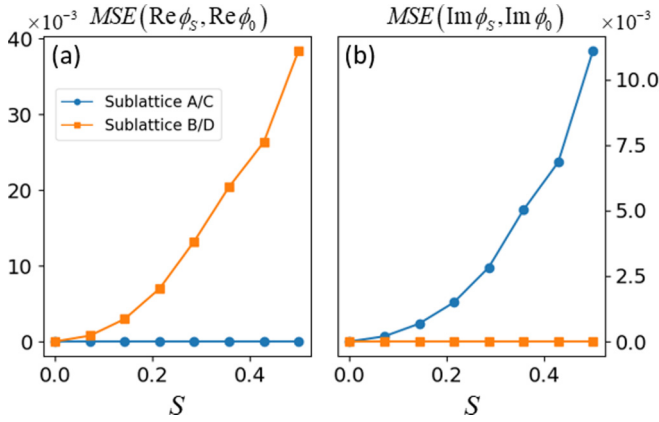


FIG. 13. Effect of the disorder strength coefficient S on the real and imaginary parts of the zero state amplitude profiles in sublattices A/C and B/D in a non-Hermitian crossed-chain Su-Schrieffer-Heeger (SSH) structure with $\gamma = 0.5$, $\tilde{a} = 2a$, and $M = 50$. The circles (squares) denote the mean value of the mean square error (MSE) for sublattice A (B) over 300 realizations of the disorder. (a) MSE of the real part of the zero-state amplitude. (b) MSE of the imaginary part of the zero-state amplitude.

We do so by considering PT -symmetry- and chirality-preserving disorder of the coupling coefficients, so that the coupling coefficients of the n th cell are

$$a_n = a + S(\tilde{a} - a) \frac{U_n}{2}, \quad (\text{G1})$$

$$\tilde{a}_n = \tilde{a} - S(\tilde{a} - a) \frac{U_n}{2}, \quad (\text{G2})$$

with U_n a random number from a uniform distribution in the range $[-1, 1]$ and $S \in \mathbb{R}$ the disorder strength parameter.

These disordered coupling coefficients are identical in all four SSH chains, so that PT symmetry is maintained for any realization if $S \leq 1 - \gamma/|\tilde{a} - a|$. The amplitudes of the topological zero, defect, and edge states on one of the axes of the crossed-chain structure are shown in Fig. 12 for 300 realizations of disorder, for $S = 0.5$, $\tilde{a} = 2a$, and $\gamma = 0.5$. Note that this is the largest disorder strength parameter for the considered coupling and gain-loss scheme according to the condition above for which PT symmetry is conserved.

It is evident from Fig. 12 that the amplitudes do not change appreciably when disorder is introduced. To quantify that, we have numerically calculated the imaginary wave numbers in each realization by exponential fitting of the amplitude profile envelope and performed an analysis on their distributions. For the zero state, we found the mean value to its distribution to be $\text{Im}\tilde{\eta}_0 \approx 0.603$, with variance $\sigma_{\tilde{\eta}_0}^2 \approx 8.657 \times 10^{-3}$ ($100 \times \sigma_{\tilde{\eta}_0}^2 / \text{Im}\tilde{\eta}_0 \approx 1.4\%$), for the edge states $\text{Im}\tilde{\eta} \approx 0.694$, with $\sigma_{\tilde{\eta}}^2 \approx 7.012 \times 10^{-3}$ ($100 \times \sigma_{\tilde{\eta}}^2 / \text{Im}\tilde{\eta} \approx 1\%$), and for the defect states $\text{Im}\tilde{\kappa} \approx 1.794$, with $\sigma_{\tilde{\kappa}}^2 \approx 28.29 \times 10^{-3}$ ($100 \times \sigma_{\tilde{\kappa}}^2 / \text{Im}\tilde{\kappa} \approx 1.6\%$). The very small variances around the respective means suggest robustness against this large disorder. Similar variances of the wave numbers in different realizations are also obtained in the Hermitian case $\gamma = 0$. Additionally, all the means converge to their zero-disorder values. This robustness demonstrates the topological nature of the crossed-chain structure also in passing to the non-Hermitian regime, as discussed in the main text.

Further indication of the topology is the persistence of the property of the zero state of having purely real amplitudes on the B/D sublattices and purely imaginary amplitudes on the A/C sublattices, with any disorder strength parameter in the above range. These numerically calculated mean square errors (MSEs) for the real and imaginary parts of sublattices A/C and B/D, with respect to an ordered amplitude profile ϕ_0 , are shown in Fig. 13. We have defined the MSE between two vectors of length n as $\text{MSE}(\vec{x}, \vec{y}) = \sum_n |x_n^2 - y_n^2|^2$.

-
- [1] M. Z. Hasan and C. L. Kane, Colloquium: Topological insulators, *Rev. Mod. Phys.* **82**, 3045 (2010).
- [2] K. van Klitzing, The quantized Hall effect, *Rev. Mod. Phys.* **58**, 519 (1986).
- [3] C. M. Bender and S. Boettcher, Real Spectra in Non-Hermitian Hamiltonians Having PT Symmetry, *Phys. Rev. Lett.* **80**, 5243 (1998).
- [4] T. Ozawa, H. M. Price, A. Amo, N. Goldman, M. Hafezi, L. Lu, M. C. Rechtsman, D. Schuster, J. Simon, O. Zilberberg *et al.*, Topological photonics, *Rev. Mod. Phys.* **91**, 015006 (2019).
- [5] F. D. M. Haldane and S. Raghu, Possible Realization of Directional Optical Waveguides in Photonic Crystals with Broken Time-Reversal Symmetry, *Phys. Rev. Lett.* **100**, 013904 (2008).
- [6] Z. Wang, Y. Chong, J. D. Joannopoulos, and M. Soljačić, Observation of unidirectional backscattering-immune topological electromagnetic states, *Nature (London)* **461**, 772 (2009).
- [7] A. J. Heeger, S. Kivelson, J. R. Schrieffer, and W.-P. Su, Solitons in conducting polymers, *Rev. Mod. Phys.* **60**, 781 (1988).
- [8] S. Ganeshan, K. Sun, and S. D. Sarma, Topological Zero-Energy States in Gapless Commensurate Aubry-André-Harper Models, *Phys. Rev. Lett.* **110**, 180403 (2013).
- [9] Y. E. Kraus and O. Zilberberg, Topological Equivalence between the Fibonacci Quasicrystal and the Harper Model, *Phys. Rev. Lett.* **109**, 116404 (2012).
- [10] A. R. Kolovsky and G. Mantica, Driven Harper model, *Phys. Rev. B* **86**, 054306 (2012).
- [11] F. D. M. Haldane, Model for a Quantum Hall Effect without Landau Levels: Condensed-Matter Realization of The ‘‘Parity Anomaly,’’ *Phys. Rev. Lett.* **61**, 2015 (1988).
- [12] H. Schomerus, Topologically protected midgap states in complex photonic lattices, *Opt. Lett.* **38**, 1912 (2013).
- [13] C. Poli, M. Bellec, U. Kuhl, F. Mortessagne, and H. Schomerus, Selective enhancement of topologically induced interface states in a dielectric resonator chain, *Nat. Commun.* **6**, 6710 (2015).
- [14] S. Longhi, Non-Hermitian gauged topological laser arrays, *Ann. Phys.* **530**, 1800023 (2018).

- [15] S. Malzard, C. Poli, and H. Schomerus, Topologically Protected Defect States in Open Photonic Systems with Non-Hermitian Charge-Conjugation and Parity-Time Symmetry, *Phys. Rev. Lett.* **115**, 200402 (2015).
- [16] S. Weimann, M. Kremer, Y. Plotnik, Y. Lumer, S. Nolte, K. G. Makris, M. Segev, M. C. Rechtsman, and A. Szameit, Topologically protected bound states in photonic parity-time-symmetric crystals, *Nat. Mater.* **16**, 433 (2017).
- [17] S. Longhi, Y. Kominis, and V. Kovanis, Presence of temporal dynamical instabilities in topological insulator lasers, *EPL* **122**, 14004 (2018).
- [18] S. Longhi, Topological Phase Transition in Non-Hermitian Quasicrystals, *Phys. Rev. Lett.* **122**, 237601 (2019).
- [19] M. A. Bandres, S. Wittek, G. Harari, M. Parto, J. Ren, M. Segev, D. N. Christodoulides, and M. Khajavikhan, Topological insulator laser: Experiments, *Science* **359**, aar4005 (2018).
- [20] Y. Yang, Z. Gao, H. Xue, L. Zhang, M. He, Z. Yang, R. Singh, Y. Chong, B. Zhang, and H. Chen, Realization of a three-dimensional photonic topological insulator, *Nature (London)* **565**, 622 (2019).
- [21] A. Dikopoltsev, T. H. Harder, E. Lustig, O. A. Egorov, J. Beierlein, A. Wolf, Y. Lumer, M. Emmerling, C. Schneider, S. Hoefling *et al.*, Topological insulator vertical-cavity laser array, *Science* **373**, 1514 (2021).
- [22] M. S. Rudner and L. S. Levitov, Topological Transition in a Non-Hermitian Quantum Walk, *Phys. Rev. Lett.* **102**, 065703 (2009).
- [23] H. Zhao, S. Longhi, and L. Feng, Robust light state by quantum phase transition in non-Hermitian optical materials, *Sci. Rep.* **5**, 17022 (2015).
- [24] M. Pan, H. Zhao, P. Miao, S. Longhi, and L. Feng, Photonic zero state in a non-Hermitian photonic lattice, *Nat. Commun.* **9**, 1308 (2018).
- [25] S. Lieu, Topological phases in the non-Hermitian su-schrieffer-heeger model, *Phys. Rev. B* **97**, 045106 (2018).
- [26] C. Yuce, Edge states at the interface of non-Hermitian systems, *Phys. Rev. A* **97**, 042118 (2018).
- [27] K. I. Imura and Y. Takane, Generalized Bloch band theory for non-Hermitian bulk-boundary correspondence, *Prog. Theor. Exp. Phys.* **2020**, 12A103 (2020).
- [28] S. Yao and Z. Wang, Edge States and Topological Invariants of Non-Hermitian Systems, *Phys. Rev. Lett.* **121**, 086803 (2018).
- [29] L. Jin and Z. Song, Solutions of PT -symmetric tight-binding chain and its equivalent Hermitian counterpart, *Phys. Rev. A* **80**, 052107 (2009).
- [30] K. I. Imura and Y. Takane, Generalized bulk-edge correspondence for non-Hermitian topological systems, *Phys. Rev. B* **100**, 165430 (2019).
- [31] R. Wang, K. L. Zhang, and Z. Song, Anderson localization induced by complex potential, *J. Phys. Commun.* **5**, 095011 (2021).
- [32] L. Jin and Z. Song, Bulk-boundary correspondence in a non-Hermitian system in one dimension with chiral inversion symmetry, *Phys. Rev. B* **99**, 081103 (2019).
- [33] D. S. Borgnia, A. J. Kruchkov, and R. J. Slager, Non-Hermitian Boundary Modes and Topology, *Phys. Rev. Lett.* **124**, 056802 (2020).
- [34] N. Okuma, K. Kawabata, K. Shiozaki, and M. Sato, Topological Origin of Non-Hermitian Skin Effects, *Phys. Rev. Lett.* **124**, 086801 (2020).
- [35] S. Longhi, Probing non-Hermitian skin effect and non-Bloch phase transitions, *Phys. Rev. Research* **1**, 023013 (2019).
- [36] S. Weidemann, M. Kremer, T. Helbig, T. Hofmann, A. Stegmaier, M. Greiter, R. Thomale, and A. Szameit, Topological funneling of light, *Science* **368**, 311 (2020).
- [37] K. Zhang, Z. Yang, and C. Fang, Correspondence between Winding Numbers and Skin States in Non-Hermitian Systems, *Phys. Rev. Lett.* **125**, 126402 (2020).
- [38] K. Zhang, Z. Yang, and C. Fang, Universal non-Hermitian skin effect in two and higher dimensions, *Nat. Commun.* **13**, 2496 (2022).
- [39] D. Obana, F. Liu, and K. Wakabayashi, Topological edge states in the Su-Schrieffer-Heeger model, *Phys. Rev. B* **100**, 075437 (2019).
- [40] A. Coutant, V. Achilleos, O. Richoux, G. Theocharis, and V. Pagneux, Topological two-dimensional Su-Schrieffer-Heeger analog acoustic networks: Total reflection at corners and corner induced modes, *J. Appl. Phys.* **129**, 125108 (2021).
- [41] H. R. Kim, M. S. Hwang, D. Smirnova, K. Y. Jeong, Y. Kivshar, and H. G. Park, Multipolar lasing states from topological corner states, *Nat. Commun.* **11**, 5758 (2020).
- [42] C. Yuce and H. Ramezani, Topological states in a non-Hermitian two-dimensional Su-Schrieffer-Heeger model, *Phys. Rev. A* **100**, 032102 (2019).
- [43] S. Imhof, C. Berger, F. Bayer, J. Brehm, L. W. Molenkamp, T. Kiessling, and R. Thomale, Topoelectrical-circuit realization of topological corner modes, *Nat. Phys.* **14**, 925 (2018).
- [44] F. Liu and K. Wakabayashi, Novel Topological Phase with a Zero Berry Curvature, *Phys. Rev. Lett.* **118**, 076803 (2017).
- [45] M. H. Teimourpour, L. Ge, D. N. Christodoulides, and R. El-Ganainy, Non-Hermitian engineering of single state two dimensional laser arrays, *Sci. Rep.* **6**, 33253 (2016).
- [46] M. Kim and J. Rho, Topological edge and corner states in a two-dimensional photonic Su-Schrieffer-Heeger lattice, *Nanophotonics* **9**, 3227 (2020).
- [47] B. Pérez-González, M. Bello, Á. Gómez-León, and G. Platero, SSH model with long-range hoppings: Topology, driving and disorder, *arXiv:1802.03973* (2018).
- [48] Z. Fu, N. Fu, H. Zhang, Z. Wang, D. Zhao, and S. Ke, Extended SSH model in non-Hermitian waveguides with alternating real and imaginary couplings, *Appl. Sci.* **10**, 3425 (2020).
- [49] S. H. Han, S. G. Jeong, S. W. Kim, T. H. Kim, and S. Cheon, Topological features of ground states and topological solitons in generalized Su-Schrieffer-Heeger models using generalized time-reversal, particle-hole, and chiral symmetries, *Phys. Rev. B* **102**, 235411 (2020).
- [50] C. Li and A. E. Miroschnichenko, Extended SSH model: Non-local couplings and non-monotonous edge states, *Physics* **1**, 2 (2019).
- [51] L. Li, Z. Xu, and S. Chen, Topological phases of generalized Su-Schrieffer-Heeger models, *Phys. Rev. B* **89**, 085111 (2014).
- [52] L. J. Lang, Y. Wang, H. Wang, and Y. D. Chong, Effects of non-Hermiticity on Su-Schrieffer-Heeger defect states, *Phys. Rev. B* **98**, 094307 (2018).
- [53] R. Chen, C. Z. Chen, B. Zhou, and D. H. Xu, Finite-size effects in non-Hermitian topological systems, *Phys. Rev. B* **99**, 155431 (2019).
- [54] S. Longhi, Bloch oscillations in tight-binding lattices with defects, *Phys. Rev. B* **81**, 195118 (2010).

- [55] A. M. Marques and R. G. Dias, Multihole edge states in Su-Schrieffer-Heeger chains with interactions, *Phys. Rev. B* **95**, 115443 (2017).
- [56] F. Munoz, F. Pinilla, J. Mella, and M. I. Molina, Topological properties of a bipartite lattice of domain wall states, *Sci. Rep.* **8**, 17330 (2018).
- [57] Y. Liu and S. Chen, Diagnosis of bulk phase diagram of non-reciprocal topological lattices by impurity modes, *Phys. Rev. B* **102**, 075404 (2020).
- [58] L. Jin, P. Wang, and Z. Song, Su-Schrieffer-Heeger chain with one pair of PT -symmetric defects, *Sci. Rep.* **7**, 5903 (2017).
- [59] P. C. Burke, J. Wiersig, and M. Haque, Non-Hermitian scattering on a tight-binding lattice, *Phys. Rev. A* **102**, 012212 (2020).
- [60] O. Bendix, R. Fleischmann, T. Kottos, and B. Shapiro, Exponentially Fragile PT Symmetry in Lattices with Localized Eigenmodes, *Phys. Rev. Lett.* **103**, 030402 (2009).
- [61] S. Garmon and K. Noba, Reservoir-assisted symmetry breaking and coalesced zero-energy modes in an open PT -symmetric Su-Schrieffer-Heeger model, *Phys. Rev. A* **104**, 062215 (2021).
- [62] Z. Xu, R. Zhang, S. Chen, L. Fu, and Y. Zhang, Fate of zero states in a finite Su-Schrieffer-Heeger model with PT symmetry, *Phys. Rev. A* **101**, 013635 (2020).
- [63] H. Zoubi and H. Ritsch, Exciton-polariton scattering as signature of defects in cold atom optical lattices, *New J. Phys.* **10**, 023001 (2008).
- [64] S. Tanaka, S. Garmon, and T. Petrosky, Nonanalytic enhancement of the charge transfer from adatom to one-dimensional semiconductor superlattice and optical absorption spectrum, *Phys. Rev. B* **73**, 115340 (2006).
- [65] H. Nakamura, N. Hatano, S. Garmon, and T. Petrosky, Quasibound States in the Continuum in a Two Channel Quantum Wire with an Adatom, *Phys. Rev. Lett.* **99**, 210404 (2007).
- [66] A. F. Sadreev and I. Rotter, S-matrix theory for transmission through billiards in tight-binding approach, *J. Phys. A-Math. Gen.* **36**, 11413 (2003).
- [67] M. G. E. Da Luz, A. S. Lupu-Sax, and E. J. Heller, Quantum scattering from arbitrary boundaries, *Phys. Rev. E* **56**, 2496 (1997).
- [68] E. N. Bulgakov and A. F. Sadreev, Bound states in the continuum in photonic waveguides inspired by defects, *Phys. Rev. B* **78**, 075105 (2008).
- [69] M. Terraneo and I. Guarneri, Distribution of resonance widths in localized tight-binding models, *Eur. Phys. J. B* **18**, 303 (2000).
- [70] J. K. Asbóth, L. Oroszlány, and A. Pályi, *A Short Course on Topological Insulators: Band Structure and Edge States in One and Two Dimensions*, Lecture Notes in Physics (Springer International, Cham, 2016), Vol. 919.
- [71] S. Ryu and Y. Hatsugai, Topological Origin of Zero-Energy Edge States in Particle-Hole Symmetric Systems, *Phys. Rev. Lett.* **89**, 077002 (2002).
- [72] C. A. Downing and G. Weick, Topological collective plasmons in bipartite chains of metallic nanoparticles, *Phys. Rev. B* **95**, 125426 (2017).
- [73] A. Stegmaier, S. Imhof, T. Helbig, T. Hofmann, C. H. Lee, M. Kremer, A. Fritzsche, T. Feichtner, S. Klembt, S. Hoeffling *et al.*, Topological Defect Engineering and PT Symmetry in Non-Hermitian Electrical Circuits, *Phys. Rev. Lett.* **126**, 215302 (2021).
- [74] P. Delplace, D. Ullmo, and G. Montambaux, Zak phase and the existence of edge states in graphene, *Phys. Rev. B* **84**, 195452 (2011).